NOAA Technical Report NESDIS 157

Report for
Dedicated JPSS VIIRS Ocean Color
Calibration/Validation Cruise:
Gulf of Mexico in April 2021

Washington, D.C.
October 2022

US DEPARTMENT OF COMMERCE
National Oceanic and Atmospheric Administration
National Environmental Satellite, Data, and Information Service

NOAA TECHNICAL REPORTS
National Environmental Satellite, Data, and Information Service

Previous NESDIS Technical Reports on the Dedicated JPSS-VIIRS-Ocean Color Calibration/Validation Cruise Series:

Report #146	November 2014	https://doi.org/10.7289/V52B8W0Z
Report #148	December 2015	https://doi.org/10.7289/V5/TR-NESDIS-148
Report #151	October 2016	https://doi.org/10.7289/V5/TR-NESDIS-151
Report #152	May 2018	https://doi.org/10.25923/scyb-qf42
Report #154	September 2019	https://doi.org/10.25923/p9de-yw97

[*] Cover image (clockwise from top left): Cruise Participants (From left to right are Roberto Arias, Mateusz Malinowski, Clemente Borgogni, Eric Stengel, Nick Tufillaro, Charles Kovach, Michael Ondrusek, David English, and Eder Herrera); VIIRS-SNPP satellite truecolor image on April 28, 2021; and the NOAA Ship *Gordon Gunter*.

NOAA Technical Report NESDIS 157

Report for
Dedicated JPSS VIIRS Ocean Color Calibration/Validation Cruise:
Gulf of Mexico in April 2021

Editor: **Jianwei Wei[1,2]***
[1]*NOAA/NESDIS Center for Satellite Applications and Research, College Park, MD 20740*
[2]*Global Science & Technology, Inc., Greenbelt, MD 20770*
*Corresponding editor: jianwei.wei@noaa.gov

Contributing authors:

Michael Ondrusek[1]*, Menghua Wang[1], Eric Stengel[1], and Charles Kovach[1,2]
[1]*NOAA/NESDIS Center for Satellite Applications and Research, College Park, MD 20740*
[2]*Global Science & Technology, Inc., Greenbelt, MD 20770*
[*]michael.ondrusek@noaa.gov

And (alphabetical by group lead last name):

Alex Gilerson*, Eder Herrera, and Mateusz Malinowski
City College of the City University of New York, New York, NY 10031
[*]gilerson@ccny.cuny.edu

Joaquim I. Goes, Helga do Rosario Gomes, and Kali McKee
Lamont Doherty Earth Observatory at Columbia University, NY 10964
[*]jig@ldeo.columbia.edu

Chuanmin Hu*, Jennifer Cannizzaro, and David English
College of Marine Science, University of South Florida, St. Petersburg, FL 33701
[*]huc@usf.edu

Sherwin Ladner[3]* and Wesley Goode[4]
[3]*University of Southern Mississippi, Stennis Space Center, MS 39529*
[4]*Naval Research laboratory, Stennis Space Center, MS 39529*
[*]sherwin.ladner@nrlssc.navy.mil

Nicholas Tufillaro* and Ivan Lalovic
College of Earth, Ocean, and Atmospheric Sciences, Oregon State University, Corvallis, OR 97331
[*]nbt@coas.oregonstate.edu

Washington, D. C.
October 2022

US DEPARTMENT OF COMMERCE
Gina M. Raimondo, Secretary

National Oceanic and Atmospheric Administration
Dr. Richard W. Spinrad, Under Secretary of Commerce for Oceans and Atmosphere and NOAA
Administrator

National Environmental Satellite, Data, and Information Service
Dr. Stephen Volz, Assistant Administrator

Table of contents

List of figures

List of tables

Preface

The ocean color science team at the National Oceanic and Atmospheric Administration (NOAA) Center for Satellite Applications and Research (STAR) is focused on the "end-to-end" production of high-quality satellite ocean color products required and expected by all NOAA line offices, as well as by external (both applied and research) users. The team has been leading the NOAA-dedicated ocean color calibration and validation (Cal/Val) cruises. The 2021 cruise is the sixth field campaign, centered on the northern Gulf of Mexico (GOM) region, where a long-term SeaPRISM system is located on the WaveCIS-6 Chevron Platform ($-90.48°W$, $+28.52°N$). This ocean color observatory is also part of NASA's Ocean Color AERONET network, providing daily ocean color and in situ atmospheric data primarily for satellite product calibration and validation. It is operated with funding and personnel from NOAA, the Naval Research Lab (NRL), and the Coastal Studies Institute (CSI) at Louisiana State University. In addition to SeaPRISM, the region is highly interested because of its water type variability and environmental and economic importance. Among others, the Mississippi River mouth is directly located to the east of the investigation area, and the Atchafalaya River is to the west. These rivers transport large amounts of sediments and nutrients to the GOM region, which contributes to the formation of the northern Gulf of Mexico Hypoxic Zone.

The cruise is focused on obtaining high-quality in situ data and producing detailed radiometric, biological, and biogeochemical data sets coincident with satellite overpasses, especially the VIIRS imagers onboard SNPP and NOAA-20. VIIRS measurements are now the primary source for NOAA operational remotely sensed ocean color data products, providing important ocean and coastal/inland water quality products. The ocean color sensors from international partners, such as the Ocean and Land Colour Instrument (OLCI) aboard the Sentinel-3 of the European Union's Copernicus mission and the Second Generation Global Imager (SGLI) aboard the Global Climate Observation Mission-Climate (GCOM-C) mission from the Japan Aerospace Exploration Agency (JAXA) will also benefit from the field observations. Researchers from STAR and external institutions participated in the field expedition. They measured the ocean color spectra (remote sensing reflectance or normalized water-leaving radiance) and water biological and biogeochemical properties, including pigment composition, phytoplankton functional types, water inherent optical properties, and underwater radiance distribution. These efforts are essential for maintaining the integrity of product data from satellite imagers, which undergo calibration changes during orbiting, and for extending the applicability of synoptic water quality data products. It is anticipated that data from the cruise will also assist in new applications, for example, remote sensing or monitoring the turnover of (low oxygen) neritic benthic waters.

Menghua Wang
Chief, Marine Ecosystems & Climate Branch; VIIRS Ocean Color Cal/Val Team Lead

Paul DiGiacomo
Chief, Satellite Oceanography & Climatology Division (SOCD), NOAA/STAR

(This page is intentionally left blank)

Abstract

The sixth NOAA-dedicated JPSS VIIRS Ocean Color Calibration/Validation Cruise was successfully conducted in the Gulf of Mexico in early 2021 when COVID-19 still threatened our society's health and safety. The NOAA Ship *Gordon Gunter* provided ship time and logistic support, and nine scientists, including one student, participated in the field campaign. It sailed off from Pascagoula, Mississippi, on April 20 and concluded in the same port on April 29. A total of 33 stations were occupied during the cruise, with continuous observations of ocean physical, optical, biological, and biogeochemical parameters along the ship tracks. At stations, the participating teams measured apparent optical properties and inherent optical properties, including remote sensing reflectance, diffuse attenuation coefficient, polarization (Stokes vector), light absorption and backscattering coefficients, phytoplankton cell counts, and fluorescence. Water samples were also collected and treated onboard to analyze phytoplankton and CDOM light absorption coefficients and suspended particulate matter. Preliminary in situ and satellite matchup data were constructed to validate VIIRS ocean color sensors onboard SNPP and NOAA-20.

1. Introduction

Satellite ocean color sensors measure the radiometric properties over global waters, including remote sensing reflectance ($R_{rs}(\lambda)$) or normalized water-leaving radiance ($nL_w(\lambda)$). $R_{rs}(\lambda)$ or $nL_w(\lambda)$ can be used to retrieve important optical, biological, and biogeochemical properties, such as chlorophyll-a (Chl-a) concentration (O'Reilly and Werdell, 2019; Wang and Son, 2016), total suspended particulate matter (SPM) (Wei et al., 2021a), diffuse attenuation coefficient at 490 nm $K_d(490)$ (Lee et al., 2005; Mueller, 2000; Wang et al., 2009a), and phytoplankton functional types (PFTs) (Moisan et al., 2017). As the remote signals are subject to significant interference from atmospheric scattering and absorption and water surface reflection, the satellite radiometric products may suffer severe uncertainties, which will eventually propagate to higher-level products, such as the Chl-a concentration product (IOCCG, 2010). Gaining confidence in the satellite product accuracy and understanding the product uncertainties is essential for long-term environmental monitoring and climate change-related studies.

NOAA has been the front-runner in supporting satellite ocean color validation and calibration since the launch of the Coastal Zone Color Scanner (CZCS) (Gordon et al., 1980; Hovis et al., 1980) in the late 1970s. Since 1991, the NOAA/STAR ocean color science team alone has conducted ship-based radiometric measurements over > 1000 stations across the global ocean (Nalli et al., 2022). In addition, NOAA played an instrumental role in developing the Marine Optical BuoY (MOBY) (Clark et al., 1997; Perez et al., 2022). MOBY has become the primary vicarious calibration reference standard for satellite ocean color sensors worldwide. Since late 2011, NOAA has launched two Visible Infrared Imaging Radiometer Suite (VIIRS) instruments onboard the SNPP and NOAA-20 satellites. The VIIRS sensors collect visible, near-infrared (NIR), and shortwave infrared (SWIR) data over the global land, atmosphere, cryosphere, and oceans. For the purpose of developing ocean color Environmental Data Records (EDRs) for open oceans and coastal/inland waters, it is critical to maintain in situ sampling for validations samples over various regions of interest and in a continuous manner.

Since 2014, the science team has led an effort, funded by the Joint Polar-orbiting Satellite System (JPSS), to conduct annual field expeditions (Ondrusek et al., 2016; Ondrusek et al., 2017; Ondrusek et al., 2019; Ondrusek et al., 2015) to validate VIIRS satellite ocean color data (Arnone et al., 2012; Arnone et al., 2014; Wang et al., 2014; Wang et al., 2013; Wei et al., 2022b), quantify the variability of in situ measurement protocols, and study the optical signatures of oceanic processes. To date, five dedicated VIIRS Cal/Val cruises have been completed. Most of them occurred in the eastern U.S. coastal oceans. The technical reports on the previous cruises are accessible online:

- Report #154, 2019 cruise, https://doi.org/10.25923/p9de-yw97
- Report #152, 2018 cruise, https://doi.org/10.25923/scyb-qf42

- Report #151, 2016 cruise, https://doi.org/10.7289/V5/TR-NESDIS-151
- Report #148, 2015 cruise, https://doi.org/10.7289/V5/TR-NESDIS-148
- Report #146, 2014 cruise, https://doi.org/10.7289/V52B8W0Z

The NOAA Office of Marine and Aviation Operations (OMAO) allocated ship time for the 2021 cruise with the NOAA Ship *Gordon Gunter* (GU2101). The primary objective of the cruise is to collect high-quality in situ optical and related biological/biogeochemical data for validating VIIRS ocean color radiometry and higher-level products. This year was a difficult time to conduct field experiments for both ship crews and the science team. Following the COVID-19 protocols, our science team was quarantined in the hotel and took COVID-19 tests before boarding the ship. The protocols also put significant limitations on the team travels and the transport of instruments to and from the ship. Despite these unprecedented difficulties, with the assistance of the ship crew, the science team successfully carried out the planned field observations in the Northern Gulf of Mexico in April 2021.

In this report, we briefly describe the implementation of the cruise and measurements of the apparent optical properties (AOPs) and inherent optical properties (IOPs), and other essential quantities measured during the cruise. We recap the field observations done by the individual science teams. We also include some preliminary results as illustrated examples of measurements in this report (Section 6). The notations and abbreviations are given in the appendix. Post-processed and quality-controlled data will typically be available after one year of this report. The final cruise dataset will be archived through NOAA/NESDIS National Centers for Environmental Information (NCEI). The final data will also be available to the ocean color community through NOAA CoastWatch (https://coastwatch.noaa.gov).

2. Investigation Area: the Gulf of Mexico

The VIIRS Cal/Val science team chose the northern Gulf of Mexico as the focus of the 2021 field campaign for multiple reasons.

Geographically, the study area is close to the Mississippi River and the Atchafalaya River, thus subject to the influence of highly turbid water plumes with high loads of sediments. Strong currents disperse and complicate the distribution and variation of SPM (D'Sa et al., 2007; Wei et al., 2021a) and colored dissolved organic matter (CDOM) in surface waters. Compared with previous cruises, the 2021 cruise has covered the most dynamic and turbid water bodies. Historically, this study area is also environmentally vulnerable. There are frequent "red tide" algae blooms that kill fish and marine mammals and cause respiratory problems in humans and domestic animals (Walsh et al., 2006). With the tremendous discharge of nitrogen and phosphorus from agricultural runoff, fossil fuel burning, and wastewater treatment effluent, a hypoxic dead zone has developed in the coastal waters along the Texas-Louisiana coastline. Hypoxia or lack of oxygen impairs bottom habitats or even leads to fish deaths (Rabalais et al., 2002).

The investigation area is bio-optically complex, much more than other regions sampled in our previous Cal/Val cruises. Figure 1 gives the monthly mean Chl-a concentration, SPM, diffuse attenuation coefficient at 490 nm, and water classes (Wei et al., 2022a) of the surface waters in the northern Gulf of Mexico in April 2021. On the one hand, the optical properties of phytoplankton are decoupled with those of other particulates, organic or inorganic, and the light absorption coefficient of CDOM. The uncertainties arising from the bio-optical modeling also translate to $R_{rs}(\lambda)$ or $nL_w(\lambda)$ products during the atmospheric correction, increasing the uncertainty in satellite radiometric products. On the other hand, the atmospheric quality of this area is not always ideal for ocean color remote sensing. Evidence showed that the presence of strongly absorbing aerosols could lead to negative or close-to-zero $R_{rs}(\lambda)$ or $nL_w(\lambda)$ at the short blue bands (Wang and Jiang, 2018; Wei et al., 2020). Last but not least, NOAA, together with other agencies, has funded the operation of an ocean color component of the Aerosol Robotic Network (AERONET-OC) in this area, which is known as the Wave-Current-Surge Information System (WaveCIS) (see Figure 4). AERONET-OC automatically measures $R_{rs}(\lambda)$ or $nL_w(\lambda)$ daily that can be aligned with concurrent satellite measurements

(Zibordi et al., 2009). The AERONET-OC and satellite matchup data play a significant role in satellite Cal/Val activities. Comparison between the AERONET-OC data and ship-based radiometric measurements offers a unique yet critical tool for evaluating the measurement uncertainties.
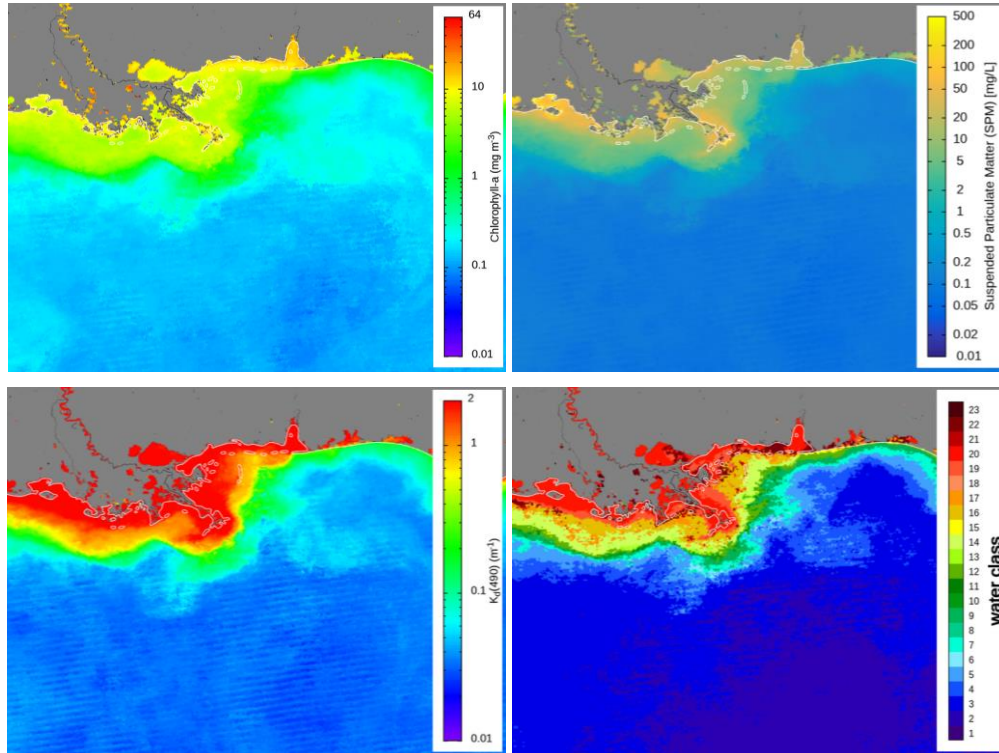
Figure 1. Monthly mean Chl-a concentration, SPM, $K_d(490)$, and water class of the surface waters in the northern Gulf of Mexico (April 2021; VIIRS-SNPP data).

Table 1. Principal investigators (PIs), participating institutions, and institution abbreviations (alphabetical order).

Name (Last, First)	Institution
Ondrusek, Michael	NOAA Center for Satellite Applications and Research (NOAA/STAR)
Ladner, Sherwin	Naval Research Laboratory (NRL)
Tufillaro, Nicholas	Oregon State University (OSU)
Gilerson, Alex	City College of New York (CCNY)
Goes, Joaquim	Lamont-Doherty Earth Observatory (LDEO)
Hu, Chuanmin	University of South Florida (USF)

3. Cruise Participants, Measurements, and Stations

3.1 Participants

Due to strict COVID-19 measures implemented by individual institutions, sending researchers to this field campaign has been challenging. Six principal investigators (Table 1) could participate in the cruise or send research staff to take water samples and measurements. Nine scientists (Table 2), including a student intern, sailed and conducted measurements. With the support of officers and crew of the NOAA Ship *Gordon Gunter* and led by Chief Scientist Mr. Michael Ondrusek, the science team carried out the planned water sampling and water measurements in a highly concerted team effort.

Table 2. List of science party personnel aboard the NOAA Ship *Gordon Gunter* (alphabetical order).

Name (Last, First)	Title	Research Group/Home Institution
Arias, Roberto	Student	University of Puerto Rico (UPR)
Borgogni, Clemente	Researcher	OSU
English, David	Researcher	USF
Herrera, Eder	Researcher	CCNY
Kovach, Charles	Researcher	NOAA/STAR
Malinowski, Matt	Researcher	CCNY
Ondrusek, Michael	Chief Scientist	NOAA/STAR
Stengel, Eric	Researcher	NOAA/STAR
Tufillaro, Nicholas	Professor	OSU

3.2 Measurements and instruments

3.2.1 Apparent optical properties

Three types of spectral radiometers were deployed during the field expedition to measure one essential apparent optical property, $R_{rs}(\lambda)$ or $nL_w(\lambda)$ (Table 3). Three types of radiometry characteristic of typical instrumental setup, capability, and data processing protocols were included. They are briefly summarized below:

- The in-water instruments consist of one above-water irradiance sensor, one in-water irradiance sensor, and one in-water radiance sensor, which were deployed from the stern of the vessel (Figure 2). While collecting the downwelling plane irradiance $E_d(\lambda)$ and upwelling radiance $L_u(\lambda)$, the profilers also measure the instrument inclination, descending rate, and temperature. After normalization to the simultaneously measured downwelling irradiance above the water surface, the $E_d(\lambda)$ and $L_u(\lambda)$ measurements allow for the derivation of $R_{rs}(\lambda)$ and $nL_w(\lambda)$. Other products, such as the diffuse attenuation coefficient $K_d(\lambda)$, can also be computed. The data processing protocol for in-water radiometry follows NASA's protocols (Mueller, 2003).
- The on-water instruments float on the water surface and measure the radiance emerging from the water (Figure 2). As it is built with a skylight-blocking apparatus (SBA) that can shield the skylight reflection off the water surface, an SBA system can measure the water-leaving radiance $L_w(\lambda)$ directly. Several recent publications have discussed the post-processing protocols for on-water radiometry (Lee et al., 2019; Wei et al., 2021b).

- The above-water instruments used in the cruise are all hand-held sensors. It measures the sky radiance ($L_{sky}(\lambda)$) and the sea surface radiance ($L_{surf}(\lambda)$) by pointing to the respective directions. To measure the downwelling irradiance, the operator needs to point the sensor to a horizontally placed plaque of a Lambertian surface. The NASA protocols (Mueller et al., 2002), along with many recent developments, provide a general guideline for data processing.

In addition to the above radiometers, a radiance distribution camera known as NuRads was deployed from the stern. A novel hyperspectral imager developed by the CCNY team was also set up for imaging the ocean surface.
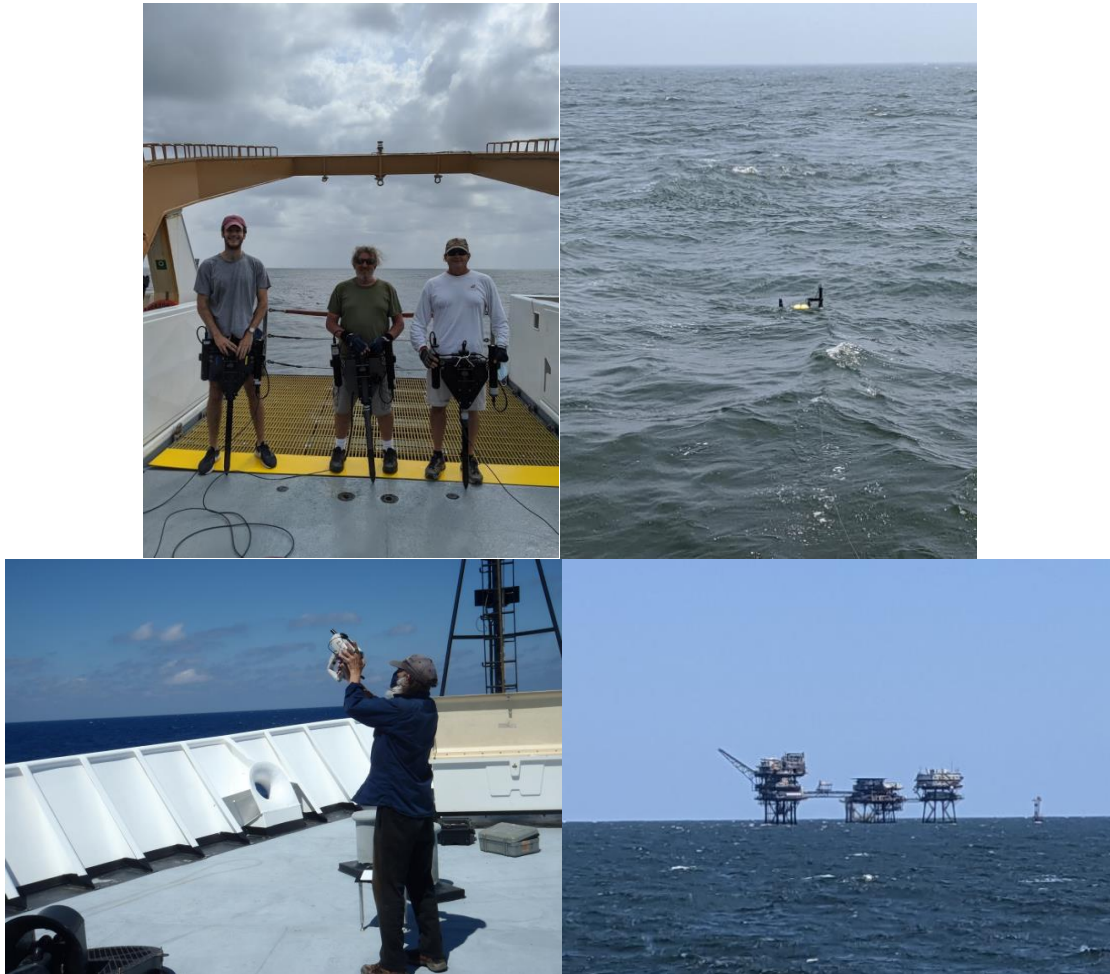
Figure 2. Deployment of HyperPro radiometers (top left), SBA instrument (top right), and an ASD instrument (bottom left). The bottom-right image shows the oil platform hosting the WaveCIS instrument. Photo credit: Michael Ondrusek

Table 3. List of spectral radiometers used in the cruise

Radiometry	Instrument	Institution
In-water	HyperPro	NOAA
	HyperPro	USF
	HyperPro	OSU
On-water	SBA	NOAA
Above-water	Spectral Evolution	OSU
	ASD	NOAA
	SVC 512	NOAA
	SVC 512	USF
	GER	CUNY

3.2.2 Inherent optical properties

The inherent optical properties, including nonwater absorption coefficient ($a_{pg}(\lambda)$), particle backscattering coefficient ($b_{bp}(\lambda)$), phytoplankton absorption coefficient ($a_{ph}(\lambda)$), and detritus absorption coefficient ($a_d(\lambda)$), were measured with both in situ instruments and water samples:

- Flow-through systems: two sets of ac-s meters (WET Labs, Inc) for $a_{pg}(\lambda)$ in hyperspectral resolution and one BB3 meter (WET Labs, Inc) for $b_{bp}(\lambda)$ at three wavelengths were set up in the wet lab, measuring the surface waters provided from a water flow-through apparatus featured with a de-bubbling mechanism.
- Water column-profiling IOP package: an ac-s meter and a BB3 meter were deployed from the winch to measure $a_{pg}(\lambda)$ and $b_{bp}(\lambda)$ profiles of the surface water column.
- Quantitative filter-pad technique (QFT): water samples were collected with the Niskin bottles at discrete water depths and then filtered with glass-fiber filters. The particulates retained on the filter pads were frozen with liquid nitrogen and then subjected to measurement with spectrophotometers once back ashore. Such measured quantities include $a_{ph}(\lambda)$, $a_d(\lambda)$, and the total particulate absorption coefficient $a_p(\lambda)$.

3.2.3 Biological and biogeochemical properties

Many biological and biogeochemical properties were measured during the cruise: Chl-a concentration, pigment composition, SPM, and phytoplankton fluorescence:

- Water samples: the science team collected water samples from the same Niskin bottles and filtered them for Chl-a, SPM, and HPLC measurements.
- Flow-through system: one CLASS ALFA and one FIRE were used to measure the phytoplankton fluorescence (Figure 3).

Figure 3. Instrument setup in the labs. Top left: flow-through system for IOPs; top right: ALFA system; bottom left: Fluorometer; bottom right: filtration lab.

3.3 Cruise stations

The ship departed from Pascagoula, Mississippi, on April 20, 2021, and returned to port on April 29, 2021 (Table 4). Field sampling is centered around the fixed station observatory WaveCIS and has also covered both turbid coastal waters and clear oceanic waters (Figure 4). Below is a brief log note of the observations (with experimental jargon):

- Day 1: Station 1. A check-out station only. The purpose is to ensure all instruments are correctly installed and operate as expected.
- Day 2: Stations halfway to WaveCIS. Chl-a = 0.1 mg m^{-3}, wind speed 15 knots. It was 95% clear skies. Some whitecaps. SNPP scenes, second SNPP overpass right on the edge of granule. Gives lower $R_{rs}(\lambda)$ between 410–499 nm compared to the first overpass.
- Day 3: NOAA-20 is a perfect match with HyperPro and a good match with WaveCIS. Chl-a = 15 mg m^{-3}, 80% clear skies, wind 20 knots. SNPP1 close to the left edge of the granule.
- Day 4: the ship had to head offshore to make water. Blue water, Chl-a = 0.2 mg m^{-3}, wind 15 knots, cloudy.
- Day 5: predicts were not very good, so the team tried to hit clearing and front. Bands of clouds move rapidly from west to east. Small cloud bands passed through right during the overpass,

obscuring Station 13. Clouds over most of the area. Wind 15 knots and hazy for Station 12 and Station 13 but improved for Station 14 and Station 15. Rough day, clouds moving fast so tried to time sampling location to clearings. SNPP radiometric products have higher values at all wavelengths. Hazy conditions.

- Day 6: Station 16, south of WaveCIS, Stations 17, 18, and 19 at WaveCIS. Station 20 East of WaveCIS clear day, good images with NOAA-20 and SNPP. Very clear skies, wind 15 knots to start the day then down to 8 knots by the last station.
- Day 7: Sampling across the front. Thought we hit a hole for NOAA-20, but there was haze, and we just missed it. The stations returned spectra with a good range of variation from Chl-a = 13 mg m^{-3} to 1.2 mg m^{-3} to 0.1 mg m^{-3}.
- Day 8: we need to head offshore to make water, and predictions called for cloudy conditions near shore. We went as far offshore as we could and still got back to port on the 10th. The NOAA-20 and two SNPP overpasses were completely clear.
- Day 9: had to pick a location within 130 nautical miles of the port entrance. Still wanted to sample across a front. The front moved from the day before but still hit it with the SNPP image. NOAA-20 was in glint.
- Day 10, near port, NOAA-20 had no data. SNPP image covered the station, but its radiometric data were high at all bands. Station has no near edges but has striping in the area.
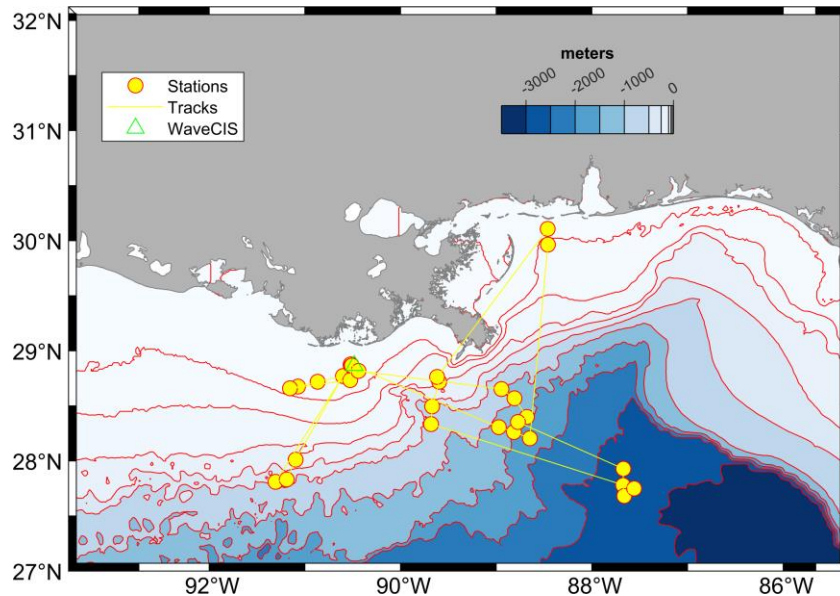
Figure 4. VIIRS Cal/Val cruise tracks and stations in the northern Gulf of Mexico in April 2021. The filled contours refer to the water depths (in meters).

Table 4. List of cruise stations, coordinates, and observation time (in Central Daylight Time or CDT).

Station	Latitude (°, North)	Longitude (°, West)	Date Local Time (CDT)
1	29.9644	−88.4593	4/20/2021 14:46
2	28.2054	−88.6476	4/21/2021 10:41
3	28.2626	−88.8149	4/21/2021 12:39
4	28.3067	−88.9727	4/21/2021 16:53
4	28.3067	−88.9727	4/21/2021 16:53
5	28.8717	−90.5219	4/22/2021 10:49
6	28.8741	−90.514	4/22/2021 12:54
7	28.8693	−90.5158	4/22/2021 14:33
8	28.8764	−90.5212	4/22/2021 16:27
9	27.81	−91.3064	4/23/2021 10:27
10	27.8317	−91.1894	4/23/2021 12:40
11	28.0114	−91.0961	4/23/2021 15:55
12	28.7707	−90.6019	4/24/2021 10:06
13	28.7187	−90.8664	4/24/2021 13:25
14	28.6753	−91.0713	4/24/2021 15:19
15	28.6595	−91.1553	4/24/2021 17:23
16	28.7338	−90.5258	4/25/2021 9:58
17	28.8631	−90.5165	4/25/2021 12:13
18	28.8627	−90.5082	4/25/2021 13:39
19	28.8659	−90.5089	4/25/2021 15:07
20	28.8172	−90.4396	4/25/2021 16:35
21	28.6526	−88.945	4/26/2021 10:04
22	28.5687	−88.8092	4/26/2021 13:07
23	28.3988	−88.6793	4/26/2021 15:32
24	28.3532	−88.7724	4/26/2021 17:31
25	27.9285	−87.6705	4/27/2021 10:17
26	27.7786	−87.6737	4/27/2021 13:38
27	27.6819	−87.6613	4/27/2021 15:27
28	27.7499	−87.5581	4/27/2021 17:55
29	28.3341	−89.6808	4/28/2021 10:13
30	28.4955	−89.6697	4/28/2013 13:22
31	28.7189	−89.5956	4/28/2021 15:22
32	28.7625	−89.6174	4/28/2021 16:48
33	30.1074	−88.4617	4/29/2021 9:41

4. Laboratory Radiometric Calibration

Pre- and/or post-cruise calibrations of several radiometers used in this cruise were conducted at the NOAA/STAR Optical Characterization Experiment Laboratory in College Park, Maryland. A NIST traceable FEL 1000 W standard irradiance lamp (#39040C, serial #667) and an Optronic Laboratories OL-455-18 integrating sphere for radiance with values traceable to NIST were used (Figure 5). A discussion of the theoretical basis for radiometric instrument calibration was included in the 2014 cruise Technical Report (Ondrusek et al., 2015) as based on primary research by Zibordi and Voss (2014) and by Johnson et al. (2014) and others. Pre-cruise calibration was conducted on February 27, 2020. This was actually a pre-cruise calibration for the scheduled March 2020 cruise that was canceled due to Covid-19. As none of the sensors were used after the February 2020 calibration and before 2021, another pre-cruise calibration was not necessary. In total, 12 irradiance sensors and 7 radiance sensors from NOAA, USF, UMB, OSU, and NASA were calibrated. The post-cruise calibration was conducted on June 3, 2021, when 12 irradiance sensors and 5 radiance sensors from NOAA, USF, UMB, OSU, and CUNY were calibrated. The NASA sensors were not utilized during the 2021 cruise, and the UMB sensors were deployed by a floating SBA apparatus. All the rest of the sensors were utilized on HyperPro profilers.
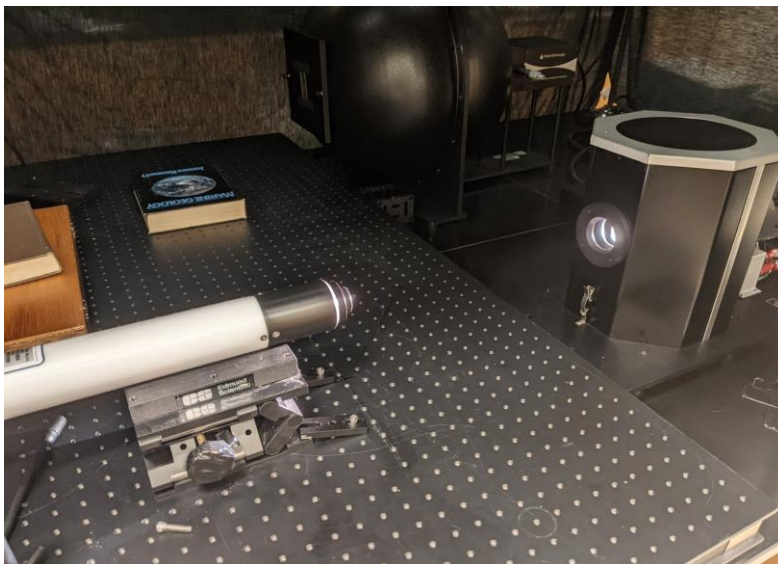
Figure 5. The Satlantic irradiance sensor is set up for calibration using an FEL lamp in the foreground. The integrating sphere used for the radiance calibrations can be seen in the background.

5. Field Activities by Individual Teams

5.1 NOAA/STAR – Michael Ondrusek, Eric Stengel, and Charles Kovach

5.1.1 Water radiometry

NOAA/STAR was responsible for organizing daily operations, station location planning, and liaison between the science party and the crew of the NOAA Ship *Gordon Gunter*. In addition to organizing the cruise operation for each station, NOAA/STAR led the simultaneous deployment of the in-water profiling radiometry instruments as described in Section 3. This included deploying, as described in Section 3.2, a Satlantic Hyperpro profiling radiometer and on-water radiometry measurements. We also participated in the above-water measurements using a Spectra Vista and a Pananalytical above-water radiometer. Also, at

each station, NOAA deployed the IOP package and operated a Microtops sunphotometer filtered seawater for HPLC pigments and fluorometric chlorophyll analysis.

The radiometric profiler operated by NOAA/STAR was a Satlantic HyperPro Profiler II package equipped with depth, temperature, and tilt sensors. The profiler system (serial number #179) was equipped with one ECO-Puck sensor (SATB2F1492) that measured fluorescence at 470 nm and 532 nm to estimate chlorophyll-a concentrations. The profiler was also equipped with a downward-looking Satlantic OCR radiance sensor (serial # 206) and an upward-pointing Satlantic OCI irradiance sensor (serial # 233). Downwelling surface irradiance was measured with an E_s sensor (serial # 234) mounted atop the grappa pole on deck. The NOAA profiler was deployed at all stations simultaneously with the USF and OSU HyperPro's utilizing the multicast deployment method where data is continuously logged while each instrument is profiled 3 to 5 times down to 15 meters. This is replicated for 3 to 5 casts at each station.

For the on-water radiometry measurements, as the University of Massachusetts Boston (UMB) team was not able to participate in the cruise, NOAA deployed UMB's SBA. The SBA instrument was deployed at every station except Stations 1 to 4 and stations 23 and 27. At Station16 and Station 17, sea conditions were too rough to permit the deployment of SBA. Figure 6 shows an example of comparison at Station 18, where the NOAA deployed two HyperPro's and one SBA.
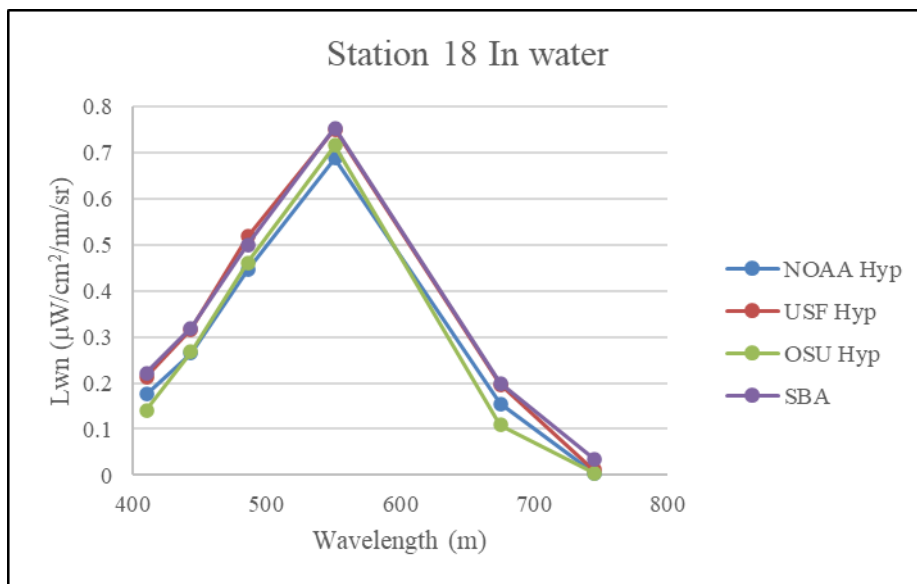
Figure 6. Normalized water-leaving radiances at Station 18 collected on April 25, 2021. Data are spectrally weighted to VIIRS visible bands. Station 18 was located near the WaveCIS site where the surface waters had chlorophyll-a concentration ranging from 4.4 to 5.1 mg/m^3.

NOAA/STAR deployed two above-water handheld instruments during the cruise. One system was the ASD HandHeld2, and the other was the Spectra Vista 512i. The ASD has a spectral range of 325 nm to 1075 nm and a spectral resolution of less than 3 nm. This unit was equipped with a built-in GPS and was equipped with fore-optics with a 10-degree FOV. The other system NOAA used was a Spectra Vista HR-512i. The NOAA HR-512i covers a spectral range of 350 nm to 1050 nm, a 3 nm spectral resolution, and an 8-degree FOV. ASD measurements were only conducted at the first two stations, while HR-512i measurements were conducted at all stations. Validation measurements were conducted on the bow simultaneously with the other team members' above-water measurements, typically while the floaters and profilers were deployed. The method of Mueller et al. (2003b) was utilized with a NOAA Spectralon white plaque with a nominal reflectance of 0.99. The water and plaque measurements were conducted at an angle of 40–45º from the

nadir and an azimuth angle to the sun of 90° to 135°. The sky was measured at a 40–45° zenith angle and at an azimuth angle to the sun of 90° to 135°.

NuRads was deployed at only 13 stations.

5.1.2 IOP Profiles

Inherent optical properties were measured at each station by lowering a package by cable down to 100 m. The package contained an ac-s (WET Labs, Inc), a BB9 (WET Labs, Inc), and a Seabird CTD. All data were collected and stored using a DH4 data handler (WET Labs, Inc).

5.1.3 Extracted fluorometric Chl-a

Chl-*a* concentrations were measured using a Turner 10 AU Fluorometer (Welschmeyer, 1994). Surface and mixed layer samples were collected in duplicate at each station from the Rosette Sampler and several times a day while underway from the flow-through system to calibrate the underway chlorophyll fluorometers. From 100 to 500 mL of seawater was filtered on a 25 mm diameter, 0.7 μm glass microfiber filter (GF/F; Whatman). The filters were frozen in liquid nitrogen for transport back to the lab, then extracted in 90% acetone in a freezer for at least 48 h. The samples were vortexed and then centrifuged for 5 min before being measured on the Turner 10 AU.

5.1.4 Suspended Particulate Matter

SPM samples were collected in duplicate from the surface waters for each station. Up to 2 liters of water were collected for each sample and processed according to techniques outlined by Hunter et al. (2006). Water samples were filtered on pre-weighed 47 mm diameter GF/F filters. The volume of the filtrate was then measured with a graduated cylinder and recorded. Filters were rinsed three times with distilled water, placed in 47 mm diameter Petri dishes, and oven dried at 60°C for 12 h, then stored in a desiccator until analysis. Filters were weighed on a Sartorius CPA 2250 balance (with a precision of 0.01 μg) and weighed at least three times until consecutive readings were less than 0.055% variable (EPA, 1971).

5.1.5 HPLC Pigments

Surface water samples were collected from each CTD rosette cast at each station. Water collected from the CTD Niskin bottles was transferred to 10 L carboys which were covered with black plastic bags to prevent high light exposure while awaiting filtration. For each sample, a known volume of water was filtered under a gentle vacuum (~127 mm Hg) onto a 25 mm diameter Whatman GF/F filter (nominal pore size ~0.7 μm). The HPLC filter samples were wrapped in aluminum foil and stored in liquid nitrogen onboard. In the laboratory, the HPLC samples were stored at -80°C until analysis and were analyzed at the NASA Goddard Space Flight Center, Ocean Ecology Laboratory. The HPLC method is modified by Van Heukelem and Thomas (2001).

5.1.6 Aerosol optical thickness

Aerosol optical thickness (AOT) was measured at 11 stations using a Microtops sunphotometer. The data are delivered for processing to NASA as part of the AERONET Marine Aerosol Network program.

5.2 NRL – Sherwin Ladner and Wesley Goode

IOP flow-through measurements were collected to address specific objectives as follows but will be used for other analyses as well:

- Characterize the spatial variability of IOPs ($a_{pg}(\lambda)$, $c_{pg}(\lambda)$, and $b_{bp}(\lambda)$) along the cruise track and how the variability impacts the uncertainty of in situ measurements at each station along with sub-pixel variability and matchup uncertainty used for VIIRS SNPP and NOAA-20 calibration and validation.
- Evaluate the vertical optical changes in coastal and offshore waters. The flow-through data at a source depth of 3 m can be different from the surface IOP which is sensed by the satellite ocean color products. Vertical profiles with CTD and IOPs can be used to evaluate the vertical changes and the effect on surface IOP validation.
- Determine the total absorption and beam attenuation properties at specific wavelengths to validate the IOPs derived from the VIIRS and NOAA-20 ocean color satellites.
- Determine the optical water mass characteristics using spectral scattering and absorption to identify the response of ocean color.
- Define coastal/shelf frontal boundaries, ocean processes, and water mass types.
- Validate VIIRS Chl-*a* and IOP products.

5.2.1 Continuous Underway Flow-through Measurements

IOPs were collected by David English (USF) continuously using an underway flow-through system on the *Gordon Gunter* designed and setup by NRL Stennis that included two Seabird hyperspectral AC-S instruments and a Seabird BB3 backscattering sensor equipped with three channels (440 nm, 532 nm, and 650 nm). It was connected to the ship's seawater flow-through system, where the water intake was located approximately 3 m below the ocean surface. A Seabird BB2F sensor (scattering at 470 and 700 nm, as well as chlorophyll fluorescence) was placed in the flow-through container with blackened walls and added to the system during the cruise to complement the BB3 measurements. To ensure stability and reliability, both AC-S instruments were placed in a controlled temperature water bath to dissipate the instruments' heat and stabilize instrument temperature (Figure 7).
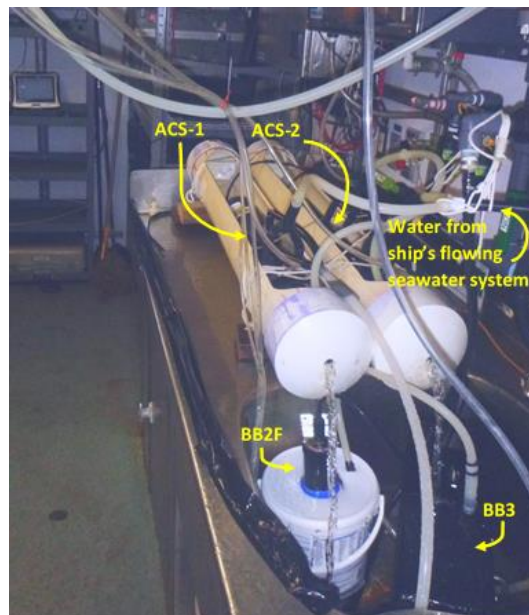
Figure 7. The NRL Stennis' IOP continuous flow-through wet lab setup on the NOAA Ship *Gordon Gunter* on GU21-01, which included two ac-s instruments, a BB3 sensor, and a BB2F sensor during the latter portion of the cruise. The two ac-s instruments were placed inside custom-designed PVC tubes to maintain a constant temperature bath during operation. The BB3

instrument was placed inside a flow cell explicitly designed for the instrument, while the BB2F was placed in an improvised flow-through container.

The two non-filtered ac-s instruments were interfaced with a Seabird DH4 data logger with additional input from the ship's GPS to provide information on location, time, and date. These inputs, mainly the timestamp, are required for merging other data not attached to the DH-4 prior to the post-processing of the ac-s data. The Seabird DH4 host software was used to combine and store all these data inputs. The data sample rate of the ac-s meters was >1 Hz. The system was started on the evening of April 20, 2021, and the DH4 output data files were saved hourly until the system was shut down at ~16:00 GMT on April 29, 2021, except for infrequent interruptions for system cleaning or computer problems.

Because of limited resources and time constraints, the two ac-s sensors were not calibrated with nano-pure water during the cruise as they were on previous validation cruises. The absorption and attenuation tubes of the ac-s sensors and the BB3 and BB2F sampling faces were cleaned several times during deployment. The BB3 and BB2F were operated with the Seabird pre-cruise calibrations.

The hyperspectral ac-s instruments (Figure 7) measured $a_{pg}(\lambda)$ and $c_{pg}(\lambda)$ from 400 nm to 742 nm at 4.0 nm spacing, and the BB3 instrument returns total volume scattering (β), volume scattering of particles (β_p), backscattering of particles $b_{bp}(\lambda)$ at three channels (440 nm, 532 nm, and 650nm). Concurrent flow-through measurements of time, latitude, and longitude, and temperature and salinity from a thermo-salinograph (CTD) will be merged and used for correction of the ac-s $a_{pg}(\lambda)$. This is important to correctly address the thermal, salinity, and scattering corrections that must be applied (Röttgers et al., 2013; WETLabs, 2011; Zaneveld et al., 1994).

5.2.2 The standard order of post-processing protocol used

- Remove sections of the data collected during the daily ac-s cleaning and pure water calibration.

- Apply temperature and salinity corrections to ac-s "*a*" data using the coincident ship thermo-salinograph temperature and salinity data.

- Temperature corrected pure water calibration data for *a* and *c*. if the calibration was performed on pre or post or during cruise else skip.

- Subtract the pure water calibration data from the in situ data if the previous step was completed else skip.

- Remove spikes in data due to bubbles, etc., using a σ filter and then interpolate

- Scattering correction (Röttgers et al., 2013; Zaneveld et al., 1994).

- Add spectral pure water absorption coefficients (Pope and Fry, 1997) to measured a_{pg} to yield a_t.

- Compute spectral scattering $b_p(\lambda) = c_{pg}(\lambda) - a_{pg}(\lambda)$.

5.3 CCNY – Alex Gilerson, Eder Herrera, and Mateusz Malinowski

The main instrument of CCNY group used for above-water observations in the validation process was GER, SpectraVista, NY. Measurements were also made with the hyperspectral polarimetric imaging system, which included a snapshot hyperspectral imager UHD485 (Cubert, Germany) and a polarization camera M2450 (Teledyne, DALSA). In addition, AOT was measured by a Microtops sunphotometer (Solar Light, PA) at five wavelengths of 380, 500, 675, 870, and 1020 nm.

5.3.1 Handheld spectroradiometer

The GER 1500, Field Portable Spectroradiometer, is a hand-held spectroradiometer designed to provide fast spectral measurements covering the UV, Visible, and NIR wavelengths from 350 to 1050 nm at 3 nm (full width half maximum, FWHM) resolution. It uses a diffraction grating with a silicon diode array that has 512 discrete detectors and provides the capacity to read 512 spectral bands. Subsequent downloads and analyses are fulfilled using a personal computer with a standard RS232 serial port and the GER 1500 licensed operating software. The GER 1500 is equipped with a standard lens with a 4° nominal field of view (FOV) for above-water observations. The GER 1500 is used in the field to calculate $R_{rs}(\lambda)$ by measuring the total radiance $L_{surf}(\lambda)$ above the sea surface, the sky radiance ($L_{sky}(\lambda)$), and the downwelling radiance ($L_d(\lambda)$) over a plaque.

The instrument has undergone radiometric and wavelength calibration in the optics mode (with the lens) at the manufacturer in March 2019 and additional tests at CCNY. Generally, due to the nature of the measurement, calibration is not necessary. The main details of the data processing are available in cruise report #4 (Ondrusek et al., 2019), which follow Mobley 99 (Mobley, 1999) approach. In addition, data were processed with the 3C model developed by Groetsch et al. (2017), which assumes spectrally dependent bias for remote sensing reflectance spectra due to the combination of the sky and sun glint.

5.3.2 Hyperspectral polarimetric imaging system

The system (Figure 8) included a snapshot hyperspectral imager with one filter wheel containing polarizing filters with different orientations and a polarization camera and another filter wheel that contained color filters. The system was operated by two laptop computers. However, the manufacturer later recognized a calibration issue with the imager related to the internal elements' instability. As a result, there will be no reliable data from the imager.
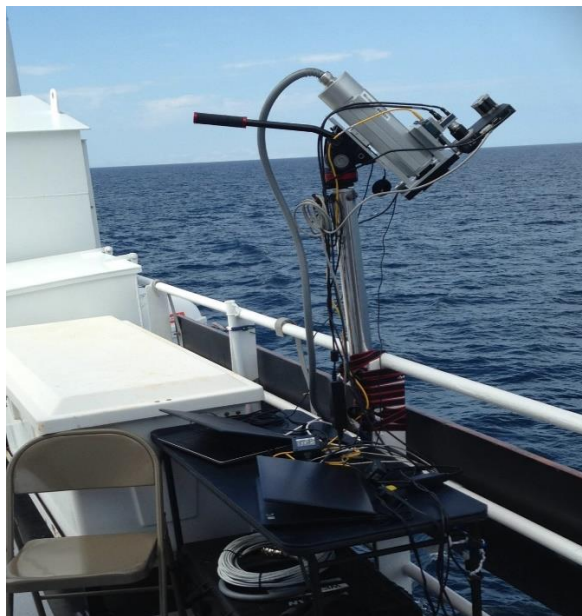
Figure 8. Snapshot hyperspectral imager with polarization camera on the ship.

5.3.3 Polarization camera

Recently released Sony image polarization sensor with 2464 (H) × 2056 (V) pixels, where each 2×2 pixel area consists of four subpixels that are equipped with polarizers oriented at 0°, 90°, 45°, and −45°,

respectively, was integrated by the Teledyne DALSA into M2450 camera and calibrated by us together with the Cubert UHD285 snapshot imager. In our implementation, it was combined with a filter wheel (Finger Lakes Instrumentation, NY) containing six color band-pass filters (AVR Optics, NY) with rectangular transmission spectra at the following center wavelengths (bandwidths) 442 (42), 494 (41), 550 (32), 655(40), 684 (24), and 775(46) nm. The camera and lens were assembled with the filter wheel to provide a rectangular FOV (HFOV $\times$ VFOV = 29.2° $\times$ 38.4°) similar to the FOV of the imager. The typical integration time was 2 ms for water measurements, 0.7 ms for sky measurements, and 0.05 ms for white plaque measurements. Videos of the water surface were acquired with a typical frame rate of about 30-40 frames/second and 8-bit digitization; standalone images were acquired with 8- and 12-bit digitization. The user interface provided by the manufacturer was integrated with the filter wheel interface to allow for the automatic acquisition of videos and images of polarization components. These images and videos were then reprocessed to get images and videos of Stokes vector components, DoLP, and angle of linear polarization (AoLP), which are further used in the analysis (Gilerson et al., 2019).

Polarimetric measurements provide additional information relevant to the VIIRS JPSS1 instrument, which has increased sensitivity to polarization. These measurements should also be helpful in the characterization of ocean wave slopes (Zappa et al., 2008) and analysis of their variability in different open ocean and coastal areas as a function of wind speed.

5.3.4 Example data and comparisons

Examples of comparison of measurements by GER and OC satellites for open ocean and coastal water stations, including data from WaveCIS AERONET-OC station, are shown in Figure 9. GER spectra were adjusted to have $R_{rs}(750) = 0$ sr^{-1}. While most of the data match reasonably well, there are some deviations, especially in coastal waters, due to higher uncertainties in satellite data processing and water variability.

A comparison of above-water GER measurements and in-water HyperPro for several stations is shown in Figure 10, mainly demonstrating a good match between above- and in-water data.

Examples of images from the polarization camera are shown in Figure 11, showing the distribution of the Stokes vector components, I, Q/I, U/I, and the degree of polarization in the field of view.

Examples of the estimated wave slope variances using polarimetric sensing with a modified algorithm (Zappa et al., 2008) at three different bands and comparison with Cox-Munk (Cox and Munk, 1954) variances are shown in Figure 12. Slope variances obviously should not depend on the band, and such small dependence is visible in Figure 12, with variances close to Cox-Munk variances.
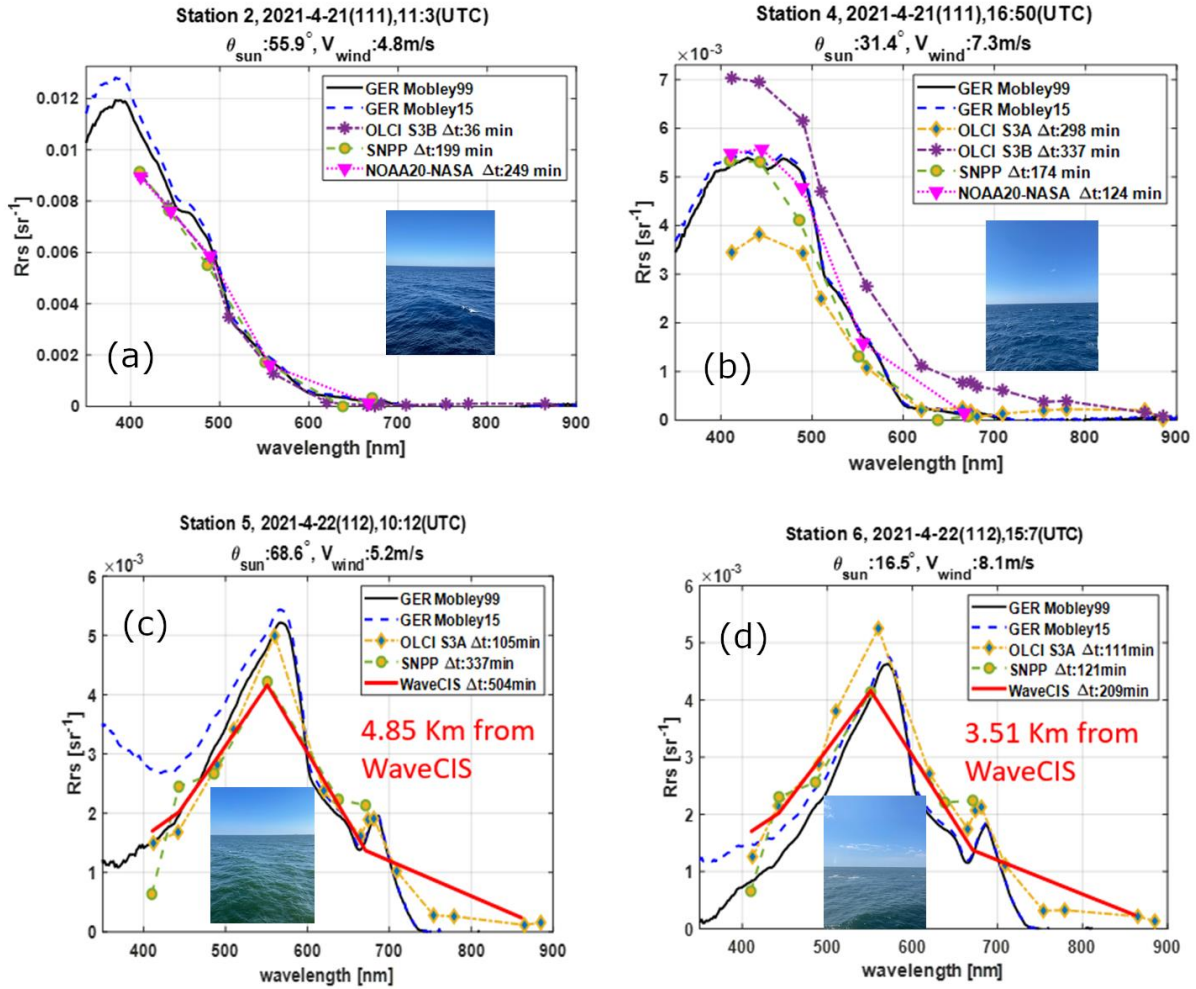
Figure 9. Comparison of measured spectra by GER with satellite data: a,b) open ocean waters, c,d) coastal waters. GER spectra are processed with reflectance coefficient from Mobley (1999) and Mobley (2015) models.
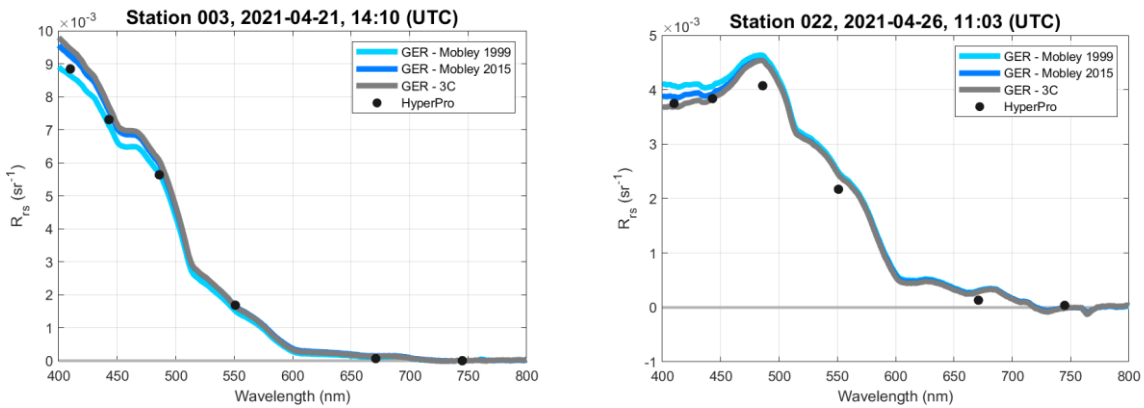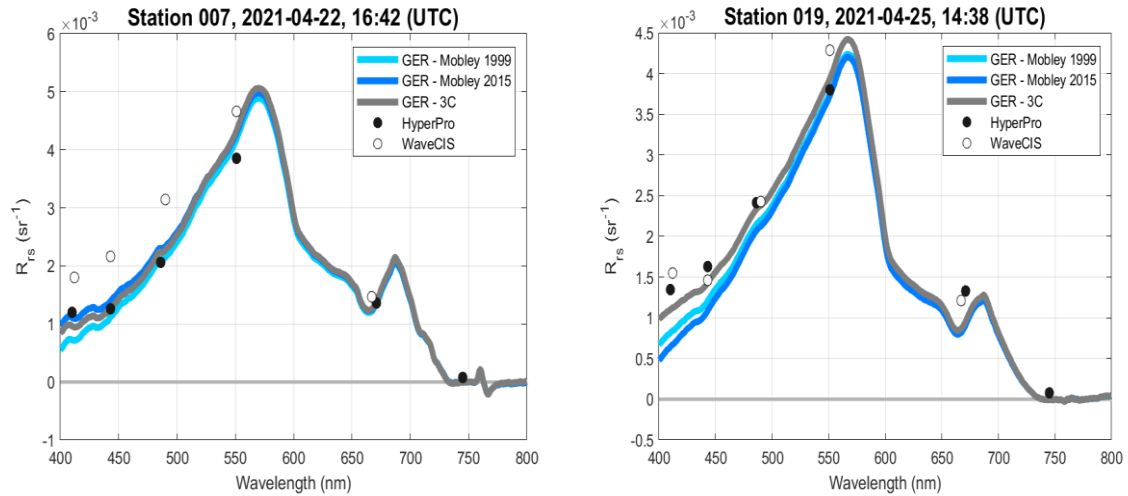
Figure 10. Comparison of measured spectra by GER above water and HyperPro below at several stations: a, b) open ocean waters, $w = 8.6$ m/s and $w = 4.2$ m/s; c, d) coastal waters, $w = 8.3$ m/s and $w = 4.8$ m/s. GER spectra are processed with reflectance coefficient from Mobley (1999), Mobley (2015), and 3C (Groetsch et al., 2017) models.
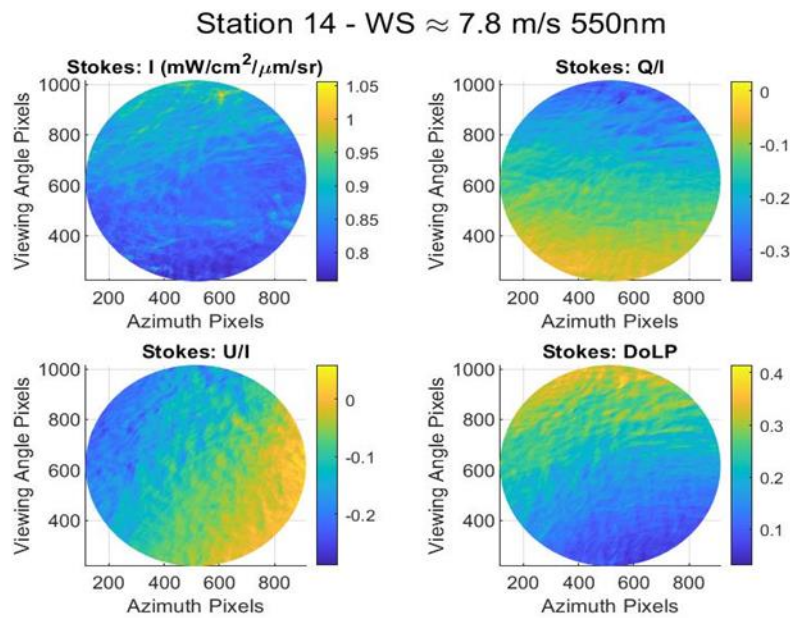
Figure 11. Example of the images from the polarization camera at Station 14.
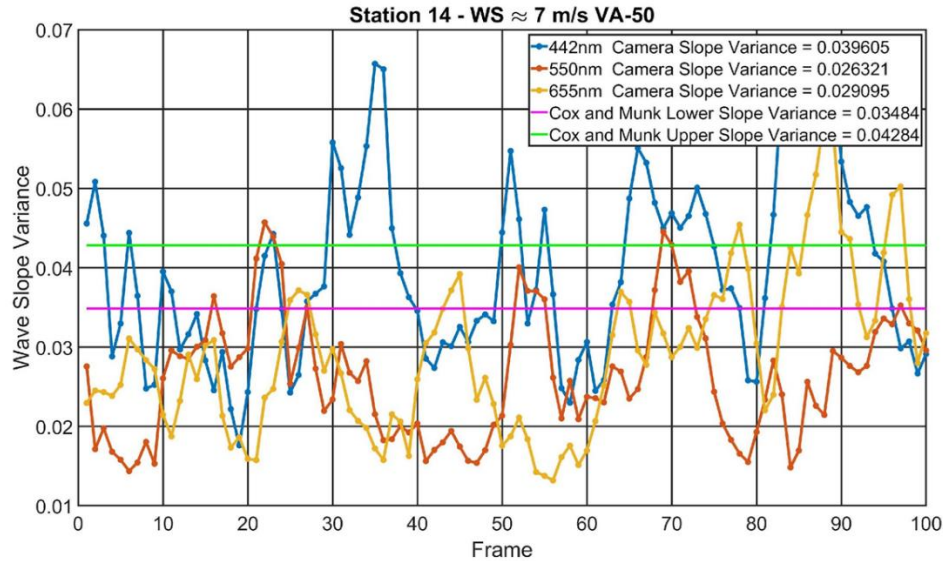
Figure 12. Estimation of wave slope variances using polarimetric sensing at Station 14.

5.4 LDEO – Joaquim I. Goes, Helga do Rosario Gomes, and Kali McKee

The LDEO group, with the support of Charles Kovach (NOAA) and Alex Gilerson (CCNY), undertook high-resolution measurements of chlorophyll, phytoplankton functional types, phytoplankton size classes, and phytoplankton photosynthetic efficiencies in near-surface (~5 m) samples from seawater that was pumped continuously through the NOAA Ship R/V *Gordon Gunter*'s uncontaminated seawater flow-through system. These measurements were repeated for discrete samples collected from 2-3 depths in the water column using a CTD rosette. In addition, samples from the three depths were pre-filtered for nutrient analyses to provide additional information about the biogeochemical conditions in the water column.

5.4.1 Discrete samples at stations

Water samples were collected from a total of 26 stations along the cruise track. At each station, seawater samples were obtained from 2-3 depths in the water column depending on the location of the subsurface Chl-a maximum for the following measurements:

- Counting, imaging, and size estimations of phytoplankton and other detrital particles using a FlowCAM (Fluid Imaging Technologies, Inc.) (Jenkins et al., 2016).

- Fluorescence-based estimates of Chl-a, CDOM, Phycobilipigments, and variable fluorescence (F_v/F_m), a measure of phytoplankton photosynthetic efficiency, using a WET Labs Custom Laser Spectrofluorometer (CLS) (Chekalyuk and Hafez, 2008; Chekalyuk et al., 2012; Goes et al., 2014).

- Measurements of F_v/F_m and the functional absorption cross-section of Photosystem II (σ_{PSII}) and Electron Transport Rates (ETR) in a mini-Fluorescence Induction and Relaxation (FIRe) (Gorbunov and Falkowski, 2004).

(1) FlowCAM-based phytoplankton identification, cell counts, and cell sizes
In addition to the microscopic analysis of phytoplankton, 5 mL aliquots of the preserved samples have been analyzed for phytoplankton community composition and size structure analysis using a FlowCAM particle imaging system equipped with a 4X objective (UPlan FLN, Olympus®) and a 300 µm FOV flow cell. FOV

flow cells ensure that the liquid passing through the flow cell is entirely encompassed within the camera's field of view. Phytoplankton cells within the preserved samples have been counted and imaged in auto-image mode with a flow rate of approximately 0.9 mL min^{-1} as specified by the manufacturer. Cells will be classified to the genus level using the Visual Spreadsheet program (v. 4.19.3, Fluid Imaging). The instrument provides the total number of particles imaged, together with the dimensions of each particle, allowing estimations of phytoplankton community structure and particle size distribution of both phytoplankton and detrital particles.

(2) Custom Laser Fluorescence (CLS) measurements of phytoplankton groups
The CLS combines high-resolution spectral measurements of blue (405 nm) and green (532 nm) laser-stimulated fluorescence with spectral deconvolution techniques to quantify the following:

- fluorescence of Chl-a (peak at 679 nm)

- three phycobilipigment types: Phycoerythrin-1 (PE-1; peak at 565 nm), Phycoerythrin-2 (PE-2; peak 578 nm), and Phycoerythrin-3 (PE-3; peak at 590 nm)

- CDOM (peak at 508 nm)

- F_v/F_m

All fluorescence values obtained are normalized to the Raman spectra of seawater and generally expressed as relative fluorescence units (RFU), whereas F_v/F_m is unitless. PE-1 type pigments are associated with blue water or oligotrophic cyanobacteria with high phycourobilin/phycoerythrobilin (PUB/PEB) ratios, PE-2 type phytoplankton with low PUB/PEB ratios are generally associated with green water cyanobacteria that usually thrive in coastal mesohaline waters, and PE-3 attributable to eukaryotic photoautotrophic cryptophytes. RFU values for Chl-a can be converted into mg m^{-3} Chl-a values using least square regressions of acetone or HPLC measured Chl-a with RFU values for Chl-a measured in an ALF.

(3) Fluorescence Induction and Relaxation (FIRe) measurements of photosynthetic competency
The FIRe instrument provides a comprehensive suite of photosynthetic and physiological characteristics of photosynthetic organisms. This technique provides a set of parameters that characterize photosynthetic light-harvesting processes, F_v/F_m, the functional absorption cross-section of PSII (σ_{PSII}), and the electron transfer rate (ETR). All optical measurements by the FIRe are sensitive, fast, and non-destructive, can be done in real time and in situ, and can provide an instant measure of the photosynthetic efficiency of the cells.

5.4.2 Underway flow-through measurements

Between stations, the CLS and the FIRe were connected in parallel to the ship's seawater flow-through system, allowing for continuous in-water measurements of phytoplankton community composition, phytoplankton size, phycobilipigment types, and photosynthetic efficiency. With the exception of a few breaks during stations and for reconditioning, both instruments were operated over the entire cruise track, providing several thousand fluorescence-based measurements of Chl-a, CDOM, F_v/F_m, and $\sigma PSII$ (Figure 13a-d).

In addition, the CLS allowed us to map (Figure 14a-c) the distribution of coastal water Cyanobacteria, open ocean Cyanobacteria, and Cryptophytes associated with different water masses in the Gulf of Mexico.

Continuous flow-through measurements of phytoplankton species distribution and cell size distribution along the cruise track will provide useful information for interpreting the optical measurements for phytoplankton function types (PFTs) over the study area. Preliminary data obtained with the flow-through instrumentation provides us with a synoptic picture of offshore and nearshore phytoplankton (Figure 15).

Synechococcus, small pennate diatoms, and other small round phytoplankton dominated in Station 3 and Station 4 in the offshore waters, whereas at Station 8, chain-forming diatoms such as *Chaetoceros* spp. and

Thallsiosira sp. were the dominated. The major species observed at Station 12 and Station 24 were the diatoms Leptocylindrus sp. *Thallasionem*a sp. *Eucampia* sp. and *Chaetoceros socialis* and some other chain-forming diatoms (Figure 16).
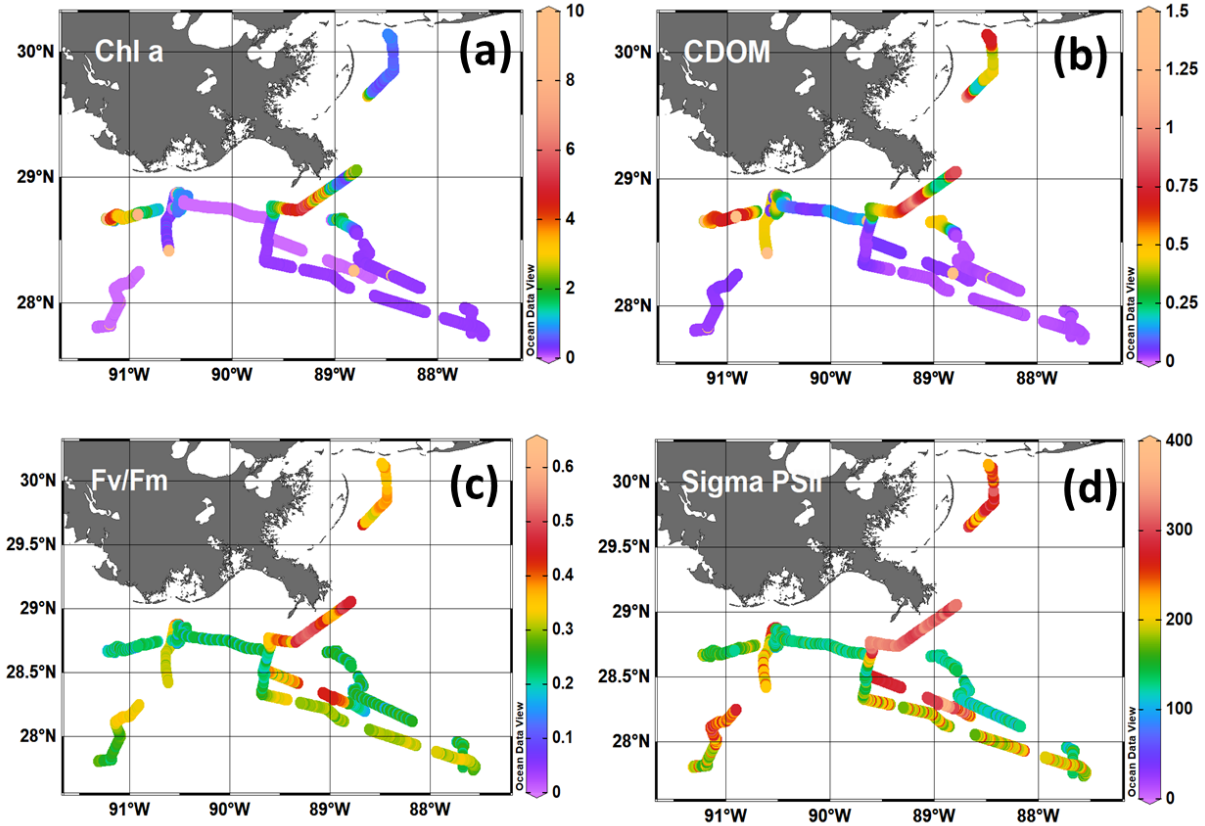
Figure 13. Distribution of Chl-a, CDOM, *Fv/Fm*, and *σPSII* along the cruise track. Data were obtained using the CLS (top panels) and FIRe (bottom panels).
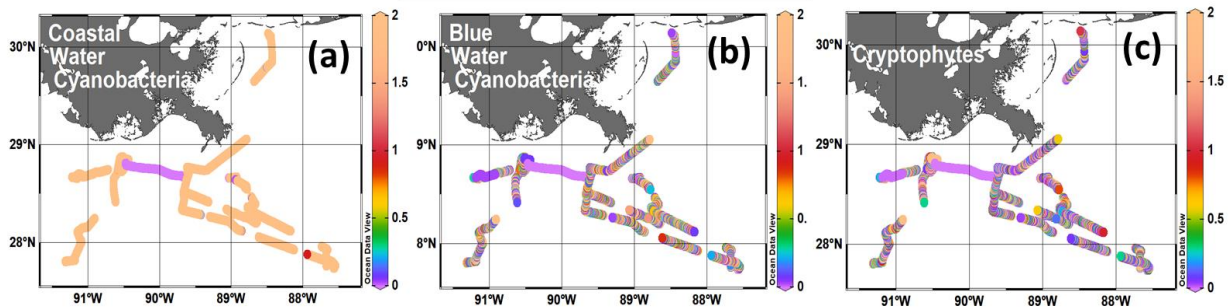
Figure 14. Distribution of (a) coastal water Cyanobacteria, (b) blue water Cyanobacteria, and (c) Cryptophytes along the cruise track.
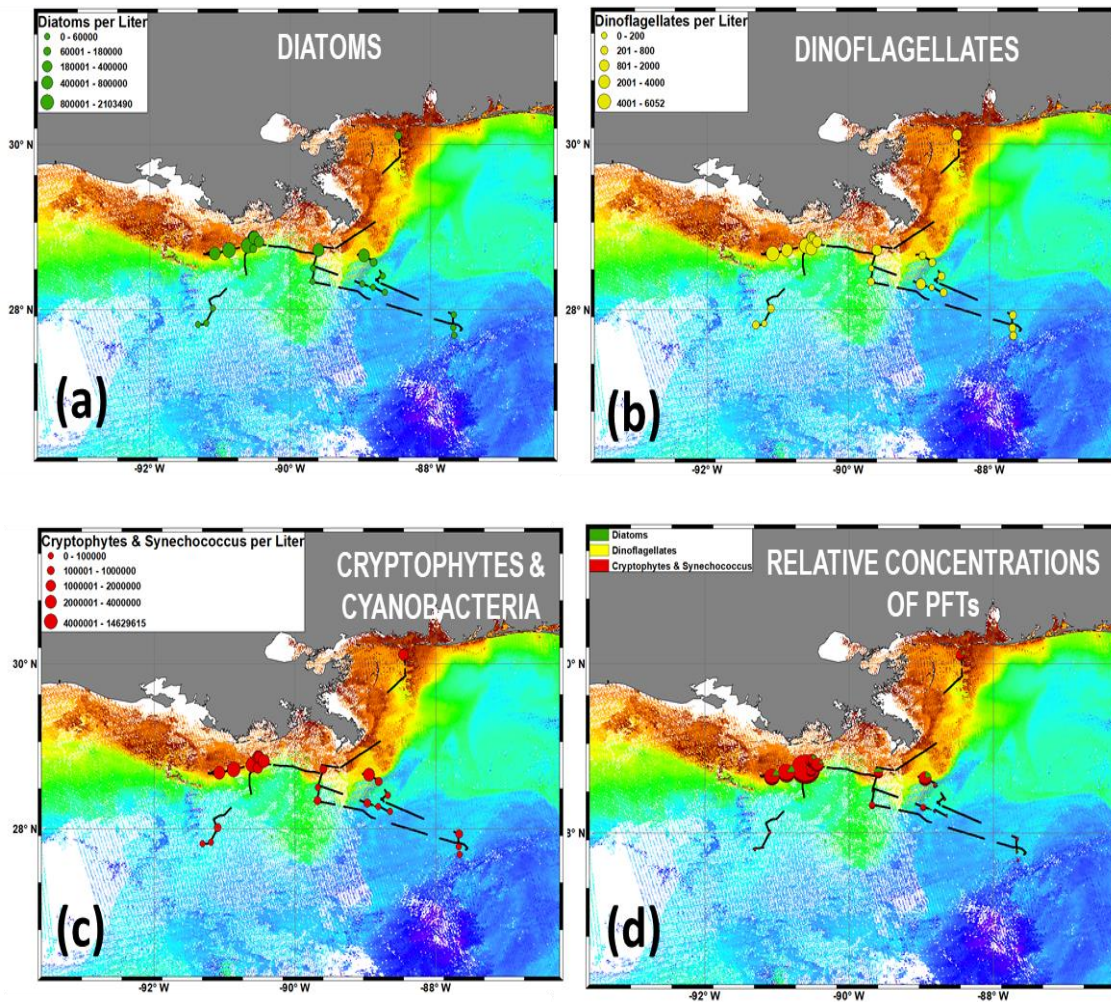
Figure 15. Distribution of (a) Diatoms, (b) Dinoflagellates, (c) Cryptophytes & Cyanobacteria, and (d) Relative percentages of PFTs at different stations occupied along the cruise track.
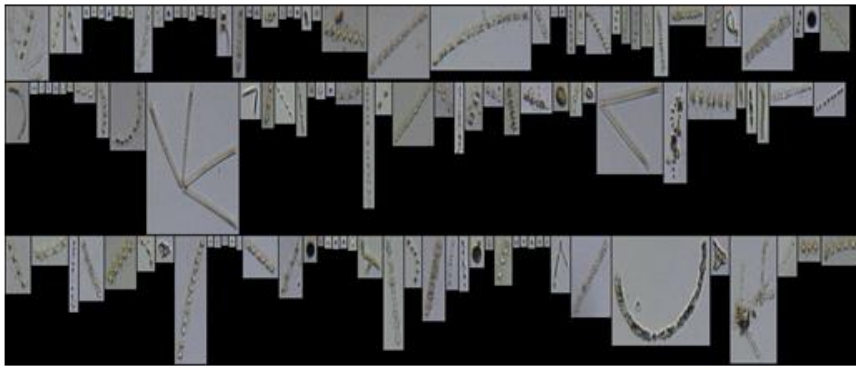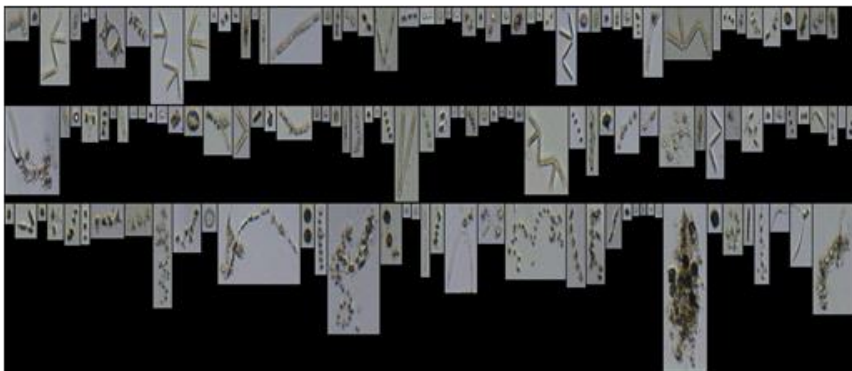
Figure 16. Major phytoplankton species at offshore and coastal stations.

5.5 USF – Chuanmin Hu, Jennifer Cannizzaro, and David English

5.5.1 Spectral absorption and pigment determinations

Measurements of the light absorption due to the particulate and dissolved components of water samples are used for understanding and modeling the underwater light field, as well as the development of remote sensing algorithms. Shortly after collection, a subset of water samples collected using the CTD rosette or surface underway system was filtered through a glass fiber filter (Whatman GF/F) to allow later spectral measurements of the light absorption by particles in the water. A portion of the filtrate was further filtered through a 0.2 μm nylon membrane filter and reserved for shore-based measurement of the spectral absorption of dissolved material, $a_g(\lambda)$, in these water samples. The extraction of the particulate pigments allows the separation of the total particulate absorption, $a_p(\lambda)$, into a living or pigmented fraction, $a_{ph}(\lambda)$, and detrital fraction, $a_d(\lambda)$ (Kishino et al., 1985). The extraction of the pigments also allows a fluorometric determination of the Chl-a concentration (Holm-Hansen and Riemann, 1978; Welschmeyer, 1994).

To verify the consistency of sample processing as processing instruments were updated, the Chl-a samples from this cruise were processed using two different fluorometers, and the particulate absorption measurements were made with two spectrophotometers. Measurements made with the newer Turner Trilogy fluorometer compared well with those made using the Turner Designs 10-AU-005 fluorometer used during the processing of previous JPSS VIIRS Ocean Color Cal/Val Cruises, and the particulate absorption measurements from the newer Perkin Elmer Lambda 850+ spectrophotometer were similar to those using the Spectrix spectrometer that was used for the previous cruises.

The CTD rosette was deployed for water sample collection at 30 stations during the cruise (Table 5). The surface waters at these stations varied from clear offshore water to highly-turbid coastal or river plume conditions, with Chl-a concentrations ranging from <0.1 to >13.0 mg m^{-3} and with CDOM absorption of 400nm light ranging from 0.019 to 1.419 m^{-1}. In addition to the samples from the surface water, a water sample from a depth near the chlorophyll maximum or from the ship's flow-through seawater system was sometimes collected. There were 31 samples collected from surface waters, 16 from waters located at depths greater than 10 m, and 12 from the ship's flowing seawater system. Example spectral absorptions from the GU21-01 water samples are shown in Figure 17.

5.5.2 Above-water remote sensing reflectance

Above-water $R_{rs}(\lambda)$ data were collected at 26 of the GU21-01 stations using a Spectra Vista Corp. (SVC) HR-512i spectroradiometer. The $R_{rs}(\lambda)$ estimate for each station is derived from multiple measurements of radiance from the water's surface, the sky, and a white-reference reflectance plaque (Carder and Steward, 1985; Mueller et al., 2003a) and incorporates a correction for reflected skylight (Mobley, 1999). The fore-optic lens of the HR-512i provided a 4° FOV. The calibrated white reference reflectance plaque was set on a platform (leveled at each station) near the ship's bow. The HR-512i viewed the sea-surface and sky (θ_w & θ_s) with viewing angles between 35° to 40° from nadir and zenith, respectively. The Θ_w angle is recorded by the HR-512i for each measurement and was used in estimating the water's skylight reflectance value during the computation of the $R_{rs}(\lambda)$ estimates.

Table 6 shows the GU21-01 measurement times and locations of the above-water $R_{rs}(\lambda)$ and HyperPro stations. The above-water $R_{rs}(\lambda)$ estimates for GU21-01 are shown in Figure 18.

Table 5. GU21-01 Optical absorption water sample times, types, and locations. All samples were collected from the CTD rosette bottles except those from the flow-through seawater system. A "●" indicates sample collection, and duplicate samples are denoted with a "2" in the table.

GU21-01 Station	sample time (UTC)	Latitude (°)	Longitude (°)	surface sample	subsurface sample	subsurface depth (m)	flow-thru seawater
1	4/20/2021	30.004	−88.476	●	●	10	
2	4/21/2021	28.215	−88.642	●	●	36	
3	4/21/2021	28.253	−88.812	●			
4	4/21/2021	28.292	−88.970	●	●	48	
5	4/22/2021	28.865	−90.508	2	●	10	
6	4/22/2021	28.863	−90.512	2	●	10	
7	4/22/2021	28.858	−90.513	●	●	10	
8	4/22/2021	28.864	−90.513	2	●	10	
9	4/23/2021	27.816	−91.282	●	●	75	
10	4/23/2021	27.835	−91.196	●	●	74	
11	4/23/2021	28.020	−91.103	●	●	48	
12	4/24/2021	28.768	−90.579	●			●
13	4/24/2021	28.721	−90.841	●			●
14	4/24/2021	28.687	−91.079	●			●
15	4/24/2021	28.660	−91.156				●
16	4/25/2021	28.745	−90.506	●			●
17	4/25/2021	28.865	−90.511	●			●
18	4/25/2021	28.861	−90.508	●			●
19	4/25/2021	28.862	−90.512				●
20	4/25/2021	28.816	−90.437	●			
21	4/26/2021	28.665	−88.926	●			●
22	4/26/2021	28.573	−88.789	●	●	10	
23	4/26/2021	28.408	−88.694	●			
25	4/27/2021	27.930	−87.660	●	●	80	
26	4/27/2021	27.765	−87.671	●	●	83	
27	4/27/2021	27.728	−87.624	●			●
29	4/28/2021	28.328	−89.665	●	2	31,55	
30	4/28/2021	28.489	−89.650	●	●	66	
31	4/28/2021	28.727	−89.607	●			●
33	4/29/2021	30.110	−88.451	●			●

Table 6. GU21-01 station times and locations for above-water $R_{rs}(\lambda)$ and HyperPro profile measurements. Above water $R_{rs}(\lambda)$ and HyperPro samplings were usually conducted within 20 minutes of each other, but the measurements were collected an hour apart at station 5. While the HyperPro was deployed at station 1, no valid $L_u(\lambda,z)$ measurements were retrievable for that station.

GU21-01 Station	sample time (UTC)	Latitude (°)	Longitude (°)	above-water	HyperPro
1	4/20/2021 19:15	29.941	−88.453	Yes	-*
2	4/21/2021 15:43	28.206	−88.647	Yes	Yes
3	4/21/2021 17:37	28.263	−88.815	Yes	Yes
4	4/21/2021 20:55	28.306	−88.973	Yes	Yes
5	4/22/2021 15:50	28.872	−90.523	Yes	Yes
6	4/22/2021 17:55	28.875	−90.515	Yes	Yes
7	4/22/2021 19:33	28.870	−90.517	Yes	Yes
8	4/22/2021 21:28	28.877	−90.522	Yes	Yes
9	4/23/2021 15:29	27.810	−91.308	-	Yes
10	4/23/2021 17:41	27.832	−91.190	-	Yes
11	4/23/2021 20:57	28.012	−91.096	-	Yes
12	4/24/2021 15:06	28.771	−90.603	-	Yes
13	4/24/2021 18:27	28.719	−90.868	Yes	Yes
14	4/24/2021 20:23	28.677	−91.072	Yes	Yes
15	4/24/2021 22:23	28.66	−91.155	-	Yes
16	4/25/2021 14:59	28.733	−90.526	Yes	Yes
17	4/25/2021 17:14	28.863	−90.517	Yes	Yes
18	4/25/2021 18:40	28.862	−90.509	Yes	Yes
19	4/25/2021 20:08	28.866	−90.51		Yes
20	4/25/2021 21:35	28.817	−90.439	Yes	Yes
21	4/26/2021 15:05	28.652	−88.946	Yes	Yes
22	4/26/2021 18:08	28.568	−88.809	Yes	Yes
23	4/26/2021 20:34	28.4	−88.68	Yes	Yes
24	4/26/2021 22:32	28.354	−88.773	-	Yes
25	4/27/2021 15:19	27.929	−87.671	Yes	Yes
26	4/27/2021 18:49	27.779	−87.674	Yes	Yes
27	4/27/2021 20:30	27.686	−87.658	Yes	Yes
28	4/27/2021 22:56	27.751	−87.557	Yes	Yes
29	4/28/2021 15:14	28.334	−89.682	Yes	Yes
30	4/28/2021 18:23	28.497	−89.670	Yes	Yes
31	4/28/2021 20:23	28.720	−89.596	Yes	Yes
32	4/28/2021 21:50	28.763	−89.617	Yes	Yes
33	4/29/2021 14:41	30.107	−88.462	Yes	Yes
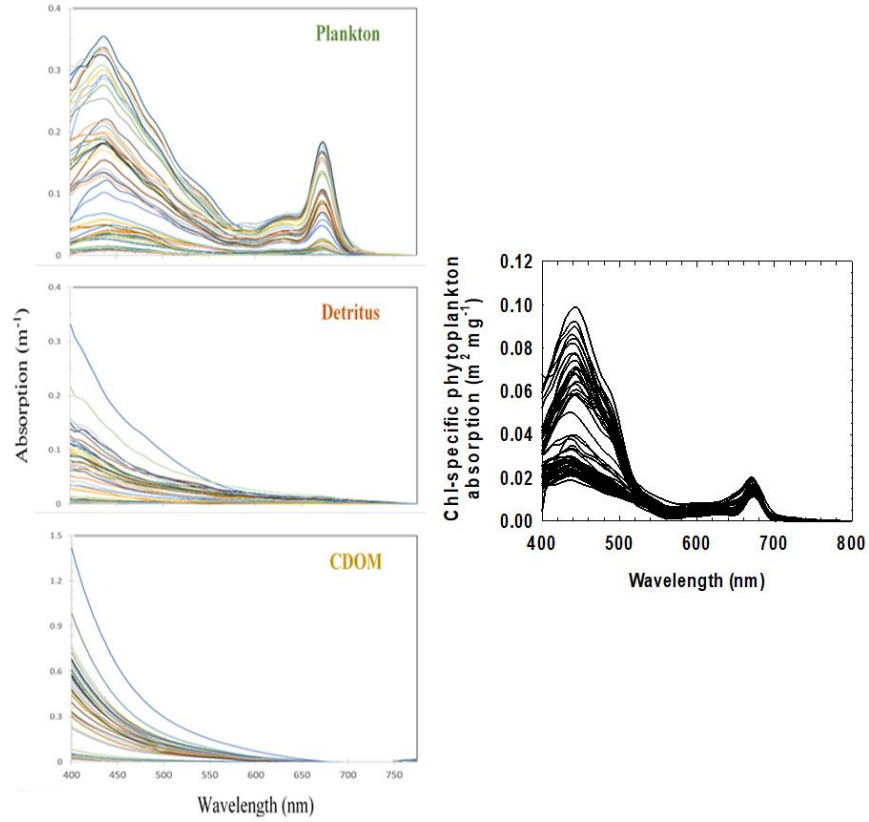
Figure 17. Spectral light absorption coefficients for phytoplankton pigments (top-left panel), non-pigmented particulate matter (i.e., detritus, middle-left panel), and colored dissolved organic matter (CDOM, in the bottom-left panel) and the chlorophyll-specific phytoplankton absorption ($a_{ph}^{*}(\lambda)$, right panel).
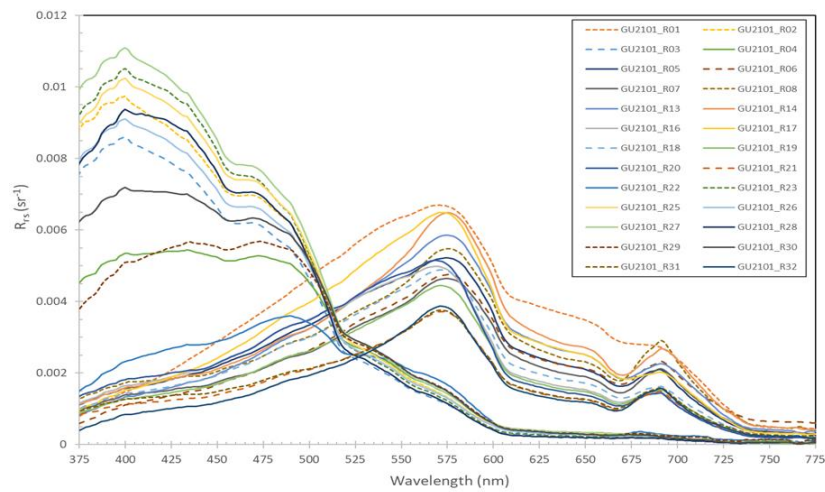
Figure 18. $R_{rs}(\lambda)$ derived from above-water HR-512i measurements during GU21-01.

5.5.3 In-water radiometry

A Satlantic HyperPro-II was deployed to collect vertical profiles of the near-surface water light field at 32 stations of GU21-01. The HyperPro-II profiler included not only $L_u(\lambda,z)$ and $E_d(\lambda,z)$ sensors, but sensors measuring pressure, temperature, conductivity, $b_b(660)$, and both Chl-*a* and CDOM fluorescence. The $L_u(\lambda,z)$ and $E_d(\lambda,z)$ measurements from multiple casts were used at each station to estimate sea surface conditions such as $L_w(\lambda,0^+)$ and $E_d(\lambda,0^+)$, $R_{rs}(\lambda)$, and $nL_w(\lambda)$. USF's HyperPro system was deployed using the manufacturer's recommended protocol (Satlantic, 2003, 2004) in coordination with the other HyperPro profilers in use during the cruise. Figure 19 shows $R_{rs}(\lambda)$ estimates derived from these HyperPro-II measurements.

While clouds and adverse conditions degraded the reliability and increased the variability of the above-water Rrs measurements for several stations, a comparison to $R_{rs}(\lambda)$ estimates derived from the HyperPro profiler showed that both the above-water and HyperPro-derived estimates had similar magnitudes and spectral shapes. For stations where the cloud cover was $< 75\%$, good agreement was observed between the estimates of $R_{rs}(\lambda)$ for several satellite wavebands (i.e., 410, 443, 486, 551, and 671 nm) derived from HyperPro-II casts and from above-water HR512i measurements, as shown in Figure 20.

5.5.4 Ad hoc flow-through measurements

During the later portion of G21-01, an improvised flow-through container containing an ECO-BB2F (WET Labs, Inc) was connected to the outflow of NOAA's ECO-BB3 tank and the NRL underway flow-through IOP system. The intent was to complement the BB3's backscattering measurements (440, 532, and 650 nm) with the BB2F's scattering (470 and 700 nm) and chlorophyll fluorescence measurements. Instrument fouling was expected to occur due to the limitations of the improvised container, and the formation of bubbles on the face of the BB2F was expected to cause significant degradation of measurement accuracy. A comparison of the BB3 and BB2F measurements suggests that while fouling did occur, there were usually 6-8 hours of measurements collected before the fouling became severe and also suggested that the default calibration values for some of the BB3 or BB2F channels should be re-evaluated.
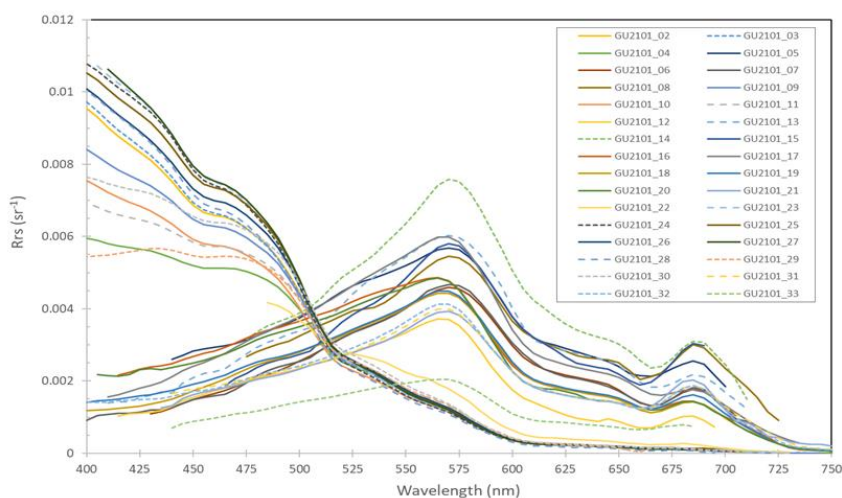
Figure 19. $R_{rs}(\lambda)$ estimated from HyperPro-II profiles at GU21-01 stations. Some estimates at wavelengths < 450 nm or > 700 nm were unreliable due to measurement noise and are not shown in this figure, and the x-axis range differs from the above-water $R_{rs}(\lambda)$ shown in Figure 18.
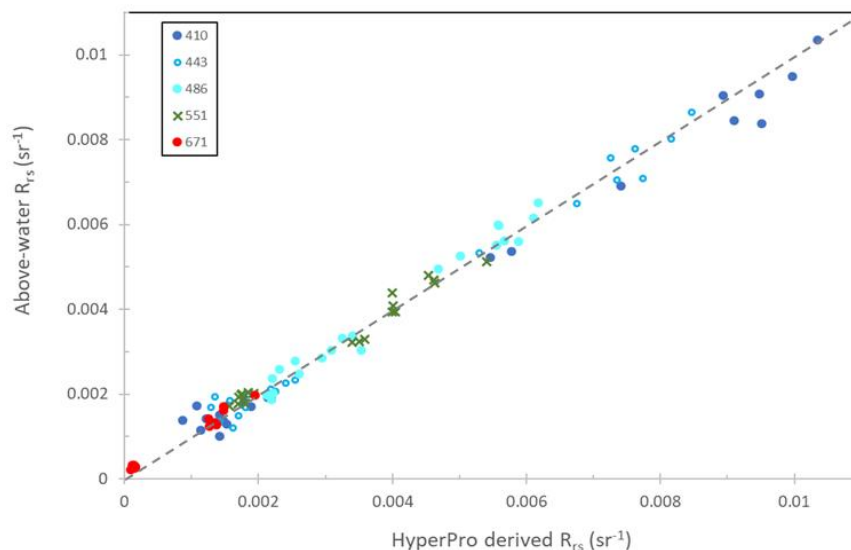
Figure 20. Comparison of HyperPro derived R_{rs} and above-water HR512i R_{rs} estimates for several VIIRS satellite wavebands at GU21-01 stations with < 75% cloud cover. The dashed line represents the 1:1 line.

5.6 OSU – Nicholas Tufillaro and Clemenente Borgogni

The OSU science team consisted of Assistant Professor Nicholas Tufillaro and one student, Clemente Borgogni. The team operated one in-water and two above-water radiometric systems. Beyond data collections at fixed stations, one of the above-water radiometers operated continuously during the daytime collecting a record of radiometric data as the ship transited from station to station. Continuous monitoring of water color throughout the daytime cruise is particularly useful in near coastal regions, which show a richness of different water types and rapid transitions between water types (Figure 21). Whereas the open ocean typically has water masses of similar color for tens of kilometers, it is not uncommon for near coastal waters to change color over hundreds of meters (Davis et al., 2007). Initial results on how these continuous ocean color measurements can complement in-water flow-through measurements, and provide additional monitoring during a cruise, are discussed.

5.6.1 Central section and the water colors in the northern Gulf of Mexico

The central section of the cruise path, as well as a guide to water types, is shown in Figure 21. The image is a high spatial resolution picture (~10 m) from Sentinel-2 taken on April 22, 2022, when the R/V *Gordon Gunter* was stationed in the vicinity of WaveCIS-6. The platform is visible from the satellite image, as shown in Figure 22. Prior to the cruise, a strong storm with gusts in excess of 30 m/s deposited more than 7 cm of rain in the region on the 13th and 14th of April. A record of the storm (wind speed and wind direction) is shown in Figure 23 based on data from Station LOPL1 — Louisiana Offshore Oil Port — located at 28.885° N and -90.025° W. During the cruise, large sediment plumes were occurring, which resulted in sharp gradients in ocean color particularly around the river mouths as shown in the Sentinel-2 image in Figure 24. This brown water mucked up boat operations, particularly its water purification system, so the captain directed the crew to limit contact with coastal sampling areas with high sediment concentrations. Hence the first stations on April 21 are all open ocean stations due south of the port that stayed clear of the Mississippi mouth. From this vantage point far from shore, the ship transited to WaveCIS-6, closer to shore, on the second day of the cruise. The third day of the cruise, 22 April 2021, was free of clouds, as shown in Figure 21, and was spent sampling near WaveCIS-6.

29
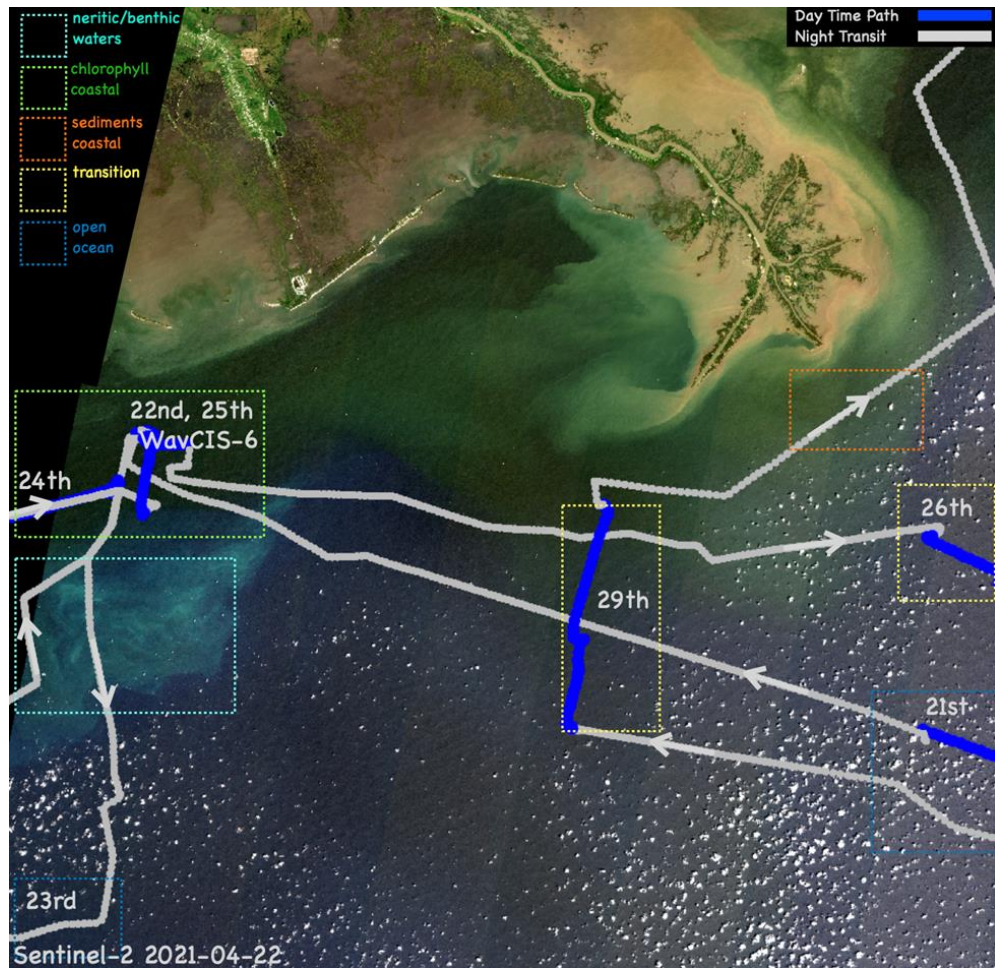
Figure 21. Map of R/V *Gordon Gunter* cruise track during 20-29 April 2021 overlaid over a Sentinel-2 image from 22 April 2021 south of Terrebonne Bay, LA.
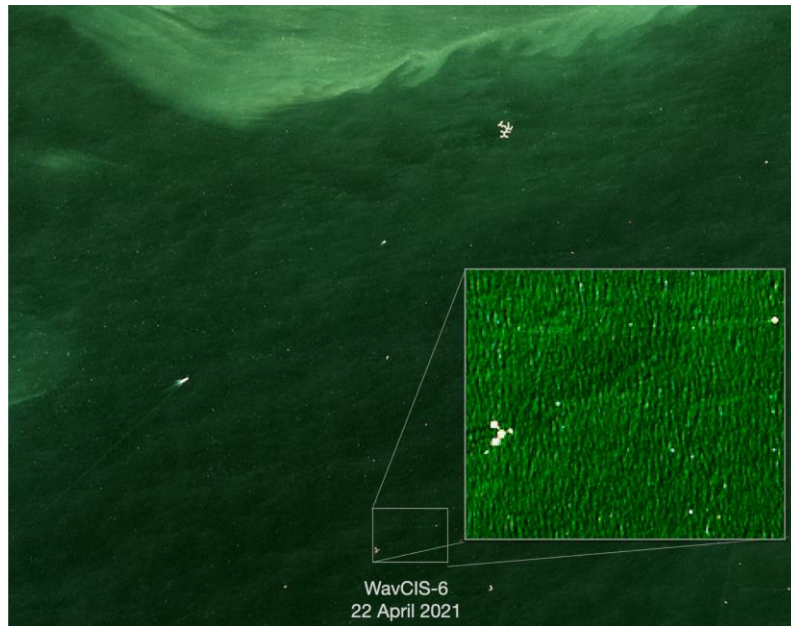
Figure 22. Image capture from Sentinel-2 of the Chevron Platform ST2B South of Terrebonne Bay, Louisiana (-90.48°W, +28.86°N) on 22 April 2021 when R/V *Gordon Gunter* was sampling.

Figure 21, Figure 22, and Figure 24 show both the richness of water colors visible and the sharp gradients between water types. Close to shore, large plumes of brownish water are seen. A bit further from shore, the water turns greener (producing a fluorescence signal in the spectra at ~ 680 nm) and is rich in CDOM, which suppresses the blue part of the spectrum. From the neritic region to the open ocean, the water turns bluer. All these water types and their spectral components are well understood. An unusual feature to notice in the water color on April 22, 2021, is a rich turquoise region due south of WaveCIS-6. This turquoise-colored water mass is also identified by NOAA's OCViewer as a 'type 7 water class' (see Figure 25) (Mikelsons and Wang, 2018; Wei et al., 2022a). We hypothesize, based on the studies of Jolliff et al. (2018b), that this water is upwelling bottom waters in the neritic zone. Figure 26 shows a sequence of remote sensing images before and after the storm. In all the imagery examined (SNPP, NOAA-20, Sentinel-3, Sentinel-2, Landsat-8) from the period, the turquoise water exists after April 14 and dissipates two weeks later by April 28. Therefore, the hypothesis is that the storm triggered the upwelling of benthic waters in the neritic region south of WaveCIS-6, which contains fine-grain sediments with a stronger scatter signal accentuating the blue end of the spectrum. Unfortunately, the cruise path crosses the turquoise water during the evening and early morning, so there is no radiometric data for these turquoise waters. This event can easily be monitored from satellite imagery, and further studies could be useful in developing applications of remote sensing imagery to help gauge and understand hypoxic events in the northern Gulf of Mexico.

31
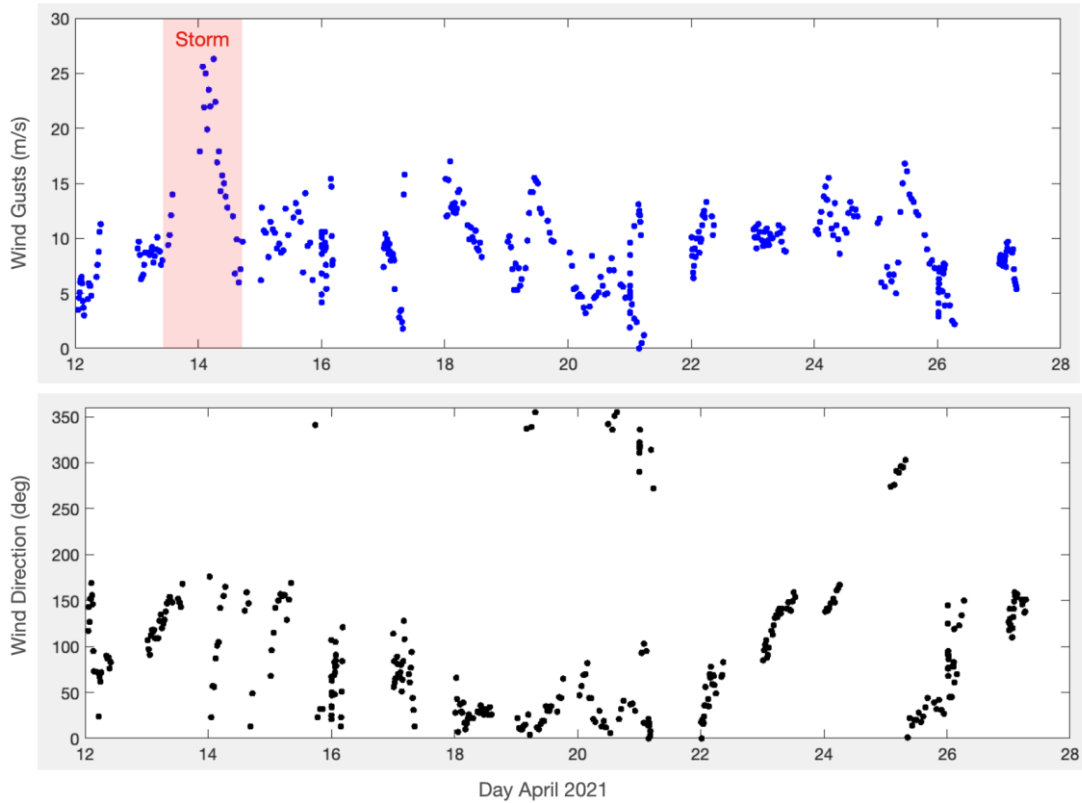
Figure 23. Time series of wind gusts and wind direction between April 12–28, 2021 from the Louisiana Offshore Oil Port located at 28.885°N and −90.025°W. A large rainstorm occurred before the cruise during April 13–14, 2021.

5.6.2 Instruments and data processing

The OSU team operated three instruments. At each station, in-water radiometric measurements were collected with HyperPro. The bove-water radiometry was collected with the Spectral Evolution PSR-1000f. Between ~10:00–16:00 CDT, a prototype ship-mounted radiometer also facing the water and sky, the 'Gybe' Sensor, was installed on Deck 2 port side (Figure 27) (Tufillaro, 2022). The basic specifications of all the instruments are displayed in Table 7.

Table 7. The main sensor specifications for the three radiometers operated by Oregon State University crew members.

	HyperOCR	SEV 1100f	Gybe Sensor
Spectral range*	350–800 @ 10 nm	320–1100 @ 3 nm	350–850 @ 10–15 nm
Integration times	4–2048 ms	8–2000 ms	0.1–8000 ms
A/D converter	16 bits	16 bits	12 bit
Sampling	3.3 nm	1.5 nm	1.8 nm
Dark Shutter	yes	yes	no

  * Calibrated range

Figure 24. The mouth of the Mississippi River feeding into the northern Gulf of Mexico, as seen by Sentinel-2 on April 22, 2021, with high sediment loads because of the rain storm a week earlier.
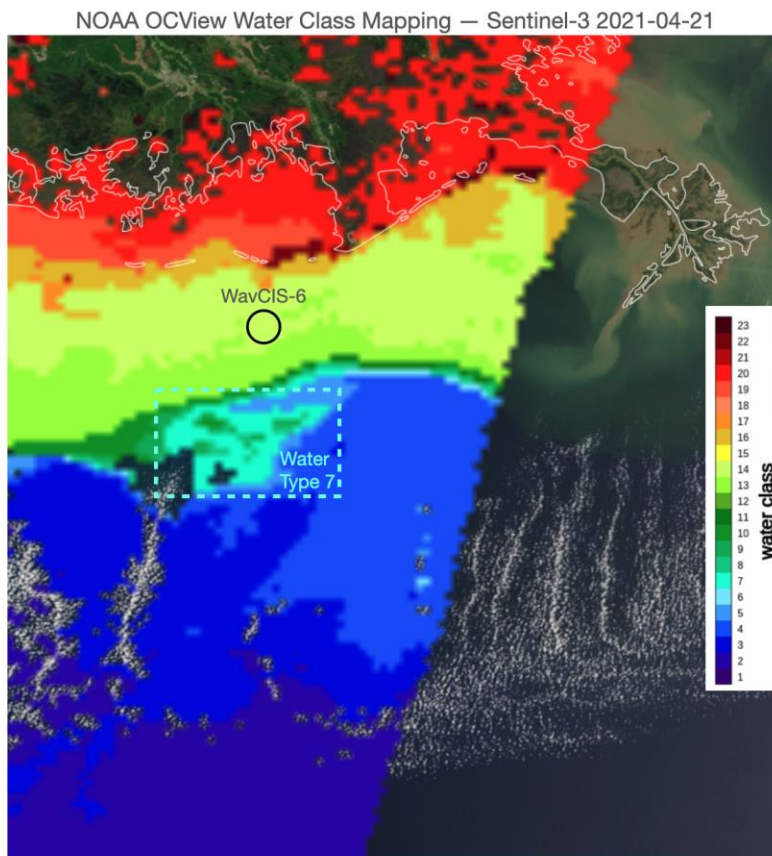
Figure 25. NOAA's Water Class Map in OCView showing a 'turquoise' water mass in the 21 April 2021 Sentinel-3 imagery south of the WaveCIS-6 sampling region.

Each group provided their HyperPro data to Mike Ondrusek at NOAA for processing to $nL_w(\lambda)$ and $R_{rs}(\lambda)$ in order to ensure a uniform processing chain for all the in-water radiance data sets. Similarly, Sherwin Lander at NRL has started uniform processing of all the above-water reflectance data based on an open source code originally created by the OSU group for the Spectral Resolution field spectrometer (OSU Remote Sensing Reflectance Codes (available at: http://aquahue.net/aquahue/software.html). The OSU code uses the Mobley protocols that utilize a single radiance sensor to measure the surface radiance and a white Spectralon plaque to estimate downwelling irradiance (Ruddick et al., 2019). In addition, the OSU group also performed direct measurements of the solar irradiance with the field spectrometer and with a calibrated optical fiber and diffuser. The operation and processing protocols for both the HyperPro and the Spectral Evolution Field Spectrometer are described in detail in previous cruise reports — see section 7.7 of Ondrusek et al. (2015), section 9.8 of Ondrusek et al. (2016), and section 11.8 of Ondrusek et al. (2017).

In this following, we will focus on the Gybe sensor since it has not previously been used by the NOAA cruise science team. Gybe is a small company in Portland, Oregon, which started in 2019 by providing water quality data to local municipal drinking water providers using spectral sensors (https://gybe.eco). Gybe is not an instrument manufacturer but instead develops sensors for its own internal use and deploys these sensors to customers (e.g., drinking water reservoirs) as part of subscription-based services providing water quality monitoring. Dr. Tufillaro is one of the founders and a science advisor of Gybe. The OSU team secured a loan of the sensor for the NOAA cruise to evaluate its utility in oceanographic research.

As shown in Figure 27, the instrument has two sensor heads that simultaneously measure the downwelling irradiance and upwelling radiance at an approximately 45-degree view angle. The FOV of the upwelling radiance sensor is 25 degrees — at the time of the cruise, the OSU team thought the FOV was 8 degrees which placed the image clear of any ship reflectances. The data is logged by a small stand single board computer (SBC), and the sensor and SBC operate off a 5V USB battery pack. Integration times are set automatically based on light conditions with a nominal rep rate of 5-10 Hz. To improve the signal-to-noise ratio (SNR), scans are typically averaged. Daily data collection results in more than 4000 individual spectral scans.

The Gybe sensors are calibrated for spectral radiance and irradiance using a halogen lamp and a transfer calibration to the (NIST traceable) SEV field spectrometer. The Gybe instrument is not laboratory grade but has sufficient accuracy in detecting changes in turbidity and pigment concentrations observed in reservoirs. Gybe typically calibrates and validates its target product values (e.g., turbidity in nephelometric turbidity unit (NTU) and chlorophyll-a concentration) with collocated USGS gauges and customer-collected water samples. OSU used the ship cruise information (shown in Figure 21) provided by Mike Ondrusek to determine the location and orientation of the Gybe Sensor, but beyond calibration and simple quality checks, no effort is made to correct for sky reflectance, glint, or reflectance from structures (i.e., the white port side of the ship). In a typical fixed-field installation, Gybe uses spectral optimization and other processing procedures to estimate the water-leaving radiance from the surface reflectance (Gege and Grötsch, 2016; Groetsch et al., 2020; Pitarch et al., 2020). In this deployment, though, we simply compute the ratio of surface leaving radiance $L_{surf}(\lambda)$ to the downwelling irradiance $E_s(\lambda)$ and attempt to correlate this quantity to features in the water expressed by the surface reflectance. There were other impairments to the signal, in particular, stray light from a 'red' ship lamp, which was also in the edge view of the sensor. We removed all data above 700 nm to minimize its contribution. Also, the Gybe instrument operation was occasionally intermittent; consequently, there were a few data dropouts during daily operations. This first deployment was a simple test to see what we could obtain. In future moving platform experiments, we can add orientation information to refine the estimation of target data products further.
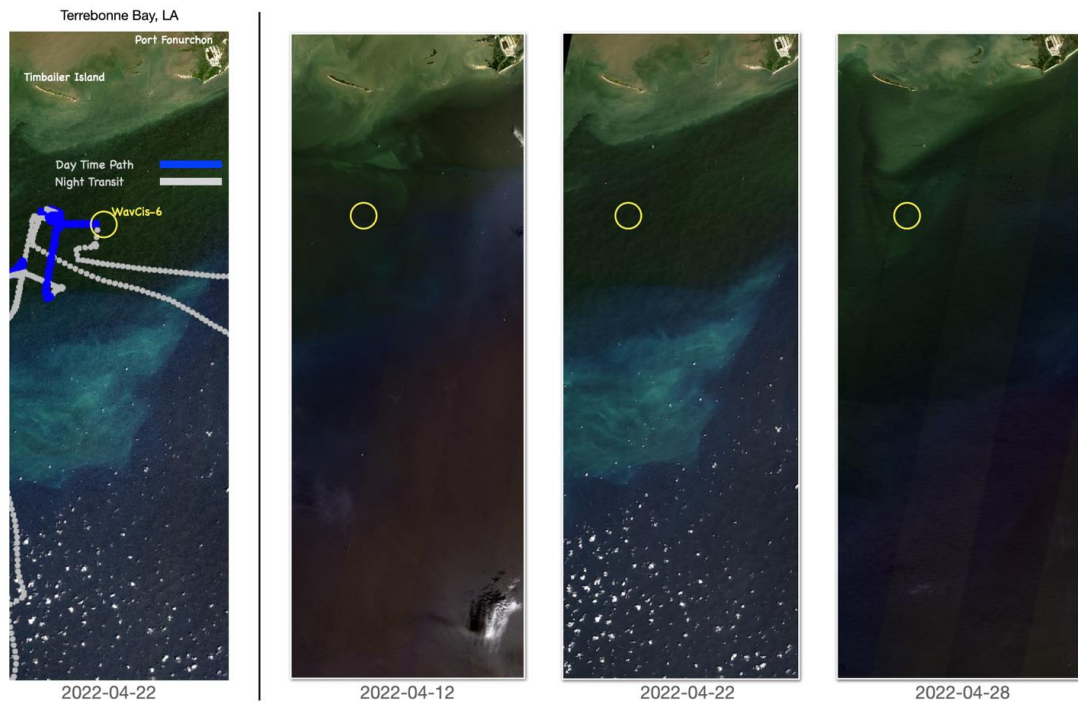
Figure 26. A sequence of images before and after the rain and windstorm showing the emergence and then dissipation of a section of 'turquoise' water in the neritic zone thought to be upwelled water due to forcing from the rainstorm on April 13, 2021. The yellow circle indicates the approximate location of the sampling region near WaveCIS-6.

Figure 27. The Gybe optical sensor mounted to the port side of the R/V *Gordon Gunter*. Clemente Borgogni is measuring the water-leaving radiance with a field spectrometer at a cruise station. The Gybe instrument is in the center of the image and has two sensor heads. The vertical black tube contains the sensor measuring the downwelling irradiance, while the black tube facing the ocean measures the upwelling surface radiance.

5.6.3 Data sets

A list of the data sets collected is presented in Table 8. In addition to the radiometric measurements, the OSU team also processed coincident satellite imagery from Sentinel-2 and Landsat-8 using the open-source software Acolite developed by Vanhellemont (2019). These two satellites are used in this report to show some higher spatial resolution imagery for illustrative points. Table 8 and Figure 21 are the primary indexes for the OSU data sets since they can map station numbers to available OSU data sets and coincident NOAA, NASA, and ESA satellite overpasses.

Table 8. A guide to the data sets collected by OSU and the coincident remote sensing imagery available.

GULF OF MEXICO — 20-29 April 2021

day	description	station	NOAA snpp/n20	ESA olci	NRL wavcis	OSU hyp	OSU sev	OSU gyb	USGS l8	ESA s2
20	port/pascagoula		√	√	1.5				-	√
		1				√	√	-		
21	open ocean		√	√	1.0				(√)	-
	south of port	2				√	-	√		
		3				√	√	√		
		4				√	√	√		
22	wavcis-6		√	√	1.5				-	√
	south of	5				√	√	√		
	Timbailer Island	6				√	√	√		
		7				√	√	√		
		8				√	√	√		
23	open ocean		-	-	-					
	south east of	9				√	-	-		
	wavcis-6	10				√	√	-		
		11				√	-	-		
24	coastal		√	√	-				-	-
	west of wavcis-6	12				√	-	√		
		13				√	√	√		
		14				√	-	√		
		15				√	-	√		
25	wavcis-6		√	√	-				-	√
		16				√	-	√		
		17				√	√	√		
		18				√	√	√		
		19				√	-	√		
		20				√	-	√		
26	open-coastal		-	√	-				-	√
		21				√	√	√		
		22				√	√	√		
		23				√	√	√		
		24				√	-	√		
27	open ocean		√	-	-				-	(√)
		25				√	√	√		
		26				√	√	√		
		27				√	√	√		
		28				√	√	√		
28	open-coastal		√	√	-				√	-
	Sackett Bank	29				√	√	√		
		30				√	√	√		
		31				√	√	√		
		32				√	-	√		
29	port/pascagoula		-	-	-				-	-
		33				√	-	-		

5.6.4 Water color transitions monitored with above water radiometry

Estimating water-leaving radiance from the side of a moving ship is a challenging problem. The Gybe sensor has no robotic parts, so the view angles are fixed relative to the ship's frame of reference. Recovering

the water-leaving radiance requires the estimation of several impairments ranging from glint, water surface sky reflectance, white caps, and variable illumination conditions. Recent work by Groetsch et al. (2020) demonstrated that spectral optimization methods could correct for some of these effects at wider view angles than called for in the NASA (Mobley) protocols used, for instance, in robotic platforms such as the SeaPRISM (Ruddick et al., 2019; Vanhellemont, 2019; Zibordi et al., 2009). As a first step, though, to gauge the possible utility of a fixed ship-mounted sensor platform, we first wanted to see if the sensor, with little or no corrections, could detect changes in water types.

Several rapid changes in water colors are visible in the remote sensing imagery during the cruise. As noted, spectral data when crossing into the 'turquoise' water would have been interesting. However, those transits happened in the evening, so there is no Gybe sensor data for that region. The next best transit showing gradients in water color would have been on the 29th when crossing from the open ocean to the coastal ocean. However, the Gybe sensor was not running on the last day of the cruise. The remaining transition is on the 26th, crossing from the coastal ocean out to the open ocean. On much of the 26th, the boat was on a South East heading and the port side Gybe sensor was facing North East at approximately the 135 degrees angle recommended by the Mobley protocol for the sun at noon, so data from that day should have minimal sky reflectance on the water surface (Mobley, 1999).

To estimate changes in water color, we choose to compute the Apparent Visible Wavelength (AVM) recently described by Vandermeulen et al. (2020). The AVM is an easy computation of the weighted spectral harmonic mean:

$$AVW = \frac{\sum\limits_{i=\lambda_1}^{\lambda_n} R_{rs}(\lambda_i)}{\sum\limits_{i=\lambda_1}^{\lambda_n} \frac{R_{rs}(\lambda_i)}{\lambda_i}} = \left[\frac{\sum\limits_{i=\lambda_1}^{\lambda_n} \lambda_i^{-1} R_{rs}(\lambda_i)}{\sum\limits_{i=\lambda_1}^{\lambda_n} R_{rs}(\lambda_i)} \right]^{-1} \tag{1}$$

which is (roughly) sensitive to the shape of the spectrum and insensitive to its overall magnitude. Perhaps surprisingly, Vandermeulen et al. found that in many cases the AVM calculated from multiple imagers and data sets consistently classified the water type based on this one number. Thus, although simple, the AVM is also useful for inspecting large data sets, such as the hyperspectral data collected by the Gybe sensor along the transit tracks.

There were four stations on the 26th, with the first three stations, 20 (~9:30 CDT), 21 (~12:00 noon), and 22 (~ 15:30 CDT), all being along the southeast track heading to the open ocean. In addition to the lab calibration of the Gybe sensor, the initial calibration gains were adjusted with a matchup to the SEV field spectrometer during the cruise. Using these cross-calibration coefficients for the gains, Figure 28 compares stations 20, 22, and 23 with the estimated AVM values. The 'green' morning spectrum shows a peak at ~680 nm, consistent with chlorophyll fluorescence. As the ship moves to the open sea, the blue end of the spectrum is boosted, as expected, and the AVM is mainly detecting the increase in the blue part of the spectrum (the left side) relative to the red part (the right side). Essentially if you think of AVM as an integrated spectral weight, the balance point of the spectrum is shifting to the left from the right (an AVM value of 500 nm to 450 nm) as the water turns bluer.

A plot of the AVM along the southeast transit to the open ocean is shown in Figure 29. Only data from 400-700 nm was used to compute the AVM. The first two stations are apparently in coastal waters with AVM indicating a transition to the open ocean water mass between 13:30–14:00 CDT, with a steep gradient. Above-water images also show the change in water color coincident with the station times. There was some data loss between 10:30–11:30 CDT and small gaps at other times due to a loose micro USB connector. However, this initial data set suggests that a fixed (non-robotic) ship-based above-water radiometer can track changes in water color with minimal signal corrections and encourages us to consider further processing of fixed ship-based radiometric data to attempt next to correct for water surface sky reflectance and additional data filtering.

37
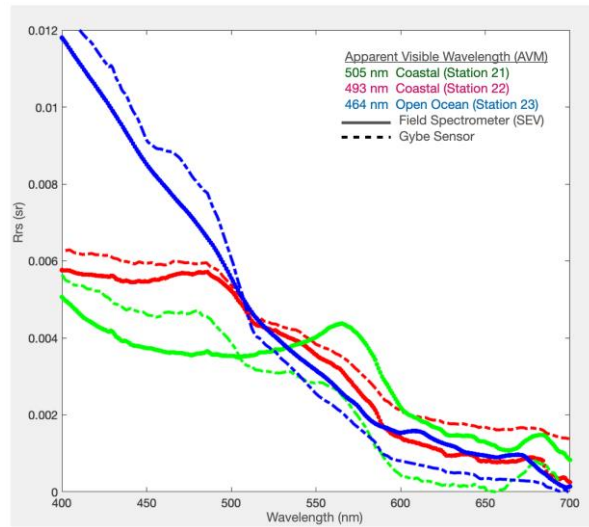
Figure 28. An estimate of the Apparent Visible Wavelength on April 26, 2021, as the R/V *Gordon Gunter* transits from coastal (Stations 21, 22) to open ocean (Station 23) waters. Also shown is a comparison of the Gybe sensor at those stations with measurements from the field spectrometer.
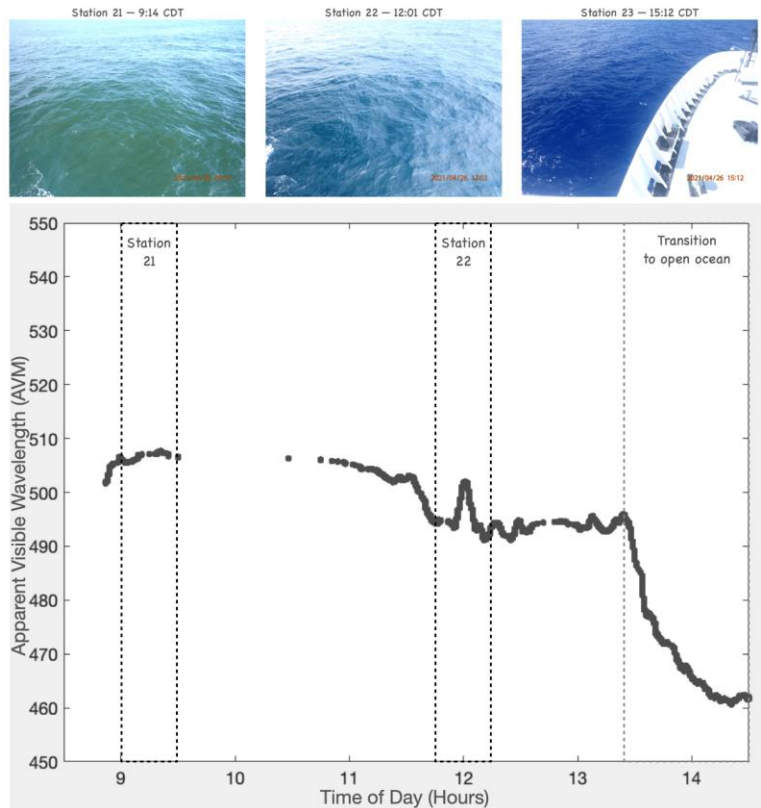
Figure 29. A plot of the Apparent Visible Wavelength [24] from the Gybe port side-mounted sensor as the R/V *Gordon Gunter* transits from coastal to open ocean on 26 April 2021. The steep drop between 13:30 and 14:00 CDT is when the ship crosses over from coastal to open ocean waters.

5.6.5 Summary

In addition to direct radiometric matches used to track and correct the calibration coefficients of operational ocean color satellites, the cruise also provided post-storm data indicating the utility of remote sensing data to detect upwelling of water in the neritic region of the Northern Gulf of Mexico — which has implications for improved understanding and monitoring of changes in the hypoxic state of waters in the Northern Gulf of Mexico (Jolliff et al., 2018a). Additionally, a low-cost non-robotic 'fixed' radiometric system was tested to gauge its possible utility of augmenting data collections continuously during the cruise, including transits. By using a single, but robust metric, the Apparent Visible Wavelength (Vandermeulen et al., 2020), we showed it is possible to track (relatively rapid) changes in ocean color while the ship is in transit. This suggests a couple of useful applications. First, remote sensing imagery is an average of the sensor footprint and thus depends on the uniformity of water color within the satellite pixel's field of view. The transiting AVM measurement provides information on the uniformity of the spatial extent — the spatial correlation — the water mass, which can be used to determine the quality of product retrials. The AVM can also be monitored in real time — along with flow-through data — to determine when the ship well with in a uniform section of water mass. Lastly, when targeting novel water mass regions, such as the 'turquoise' water during this cruise, the real time monitoring of the AVM can help ensure that a station is on target.

6. Validation of VIIRS Ocean Color Data with In Situ Observations

Figure 30 shows a comparison of $nL_w(\lambda)$ by calibrated instruments, including three profiling HyperPros, one floating SBA, and four handheld above-water instruments. Not all instruments were deployed at each station, depending on conditions or time constraints. Intercomparisons of the in situ $nL_w(\lambda)$ measurements from multiple methods at each station are shown to provide an estimate of in situ measurement variability. For each station, $nL_w(\lambda)$ spectra are displayed for each instrument along with the average $nL_w(\lambda)$ of all instruments. The number of instruments varies for each station. Since spectral resolutions differ between instruments, all data were spectrally weighted to VIIRS spectral response function. For each station, instruments that gave measurements beyond one standard deviation (σ) from the average of all instrument measurements at that station were omitted from the results. Table 9 gives the cruise average percent difference of individual instrument $nL_w(\lambda)$ relative to the average $nL_w(\lambda)$ of all instruments at each station.

Table 9. The average across all stations of the percent difference (%) of individual instrument $nL_w(\lambda)$ relative to the average $nL_w(\lambda)$ of all instruments.

Band	Hyper Pro	Above	NOAA Hyp	USF Hyp	OSU Hyp	SBA	GER	USF SVC	NOAA SVC	OSU SEV
410	−4.2	51.5	1.7	8.4	−22.9	12.6	−2.9	1.5	31.2	176.0
443	0.2	37.2	−2.0	9.1	−6.6	11.1	−5.0	−2.2	21.7	134.2
486	−0.5	31.3	−2.7	5.0	−3.7	7.8	−3.8	4.8	15.5	108.9
551	−0.3	57.8	−2.8	2.8	−0.9	5.0	−3.8	5.9	12.9	216.1
671	−6.6	396.0	10.8	13.6	−44.1	23.6	−35.1	46.0	62.3	1510.6
Avg410-551	−1.2	44.4	−1.4	6.3	−8.5	9.1	−3.9	2.5	20.3	158.8

39
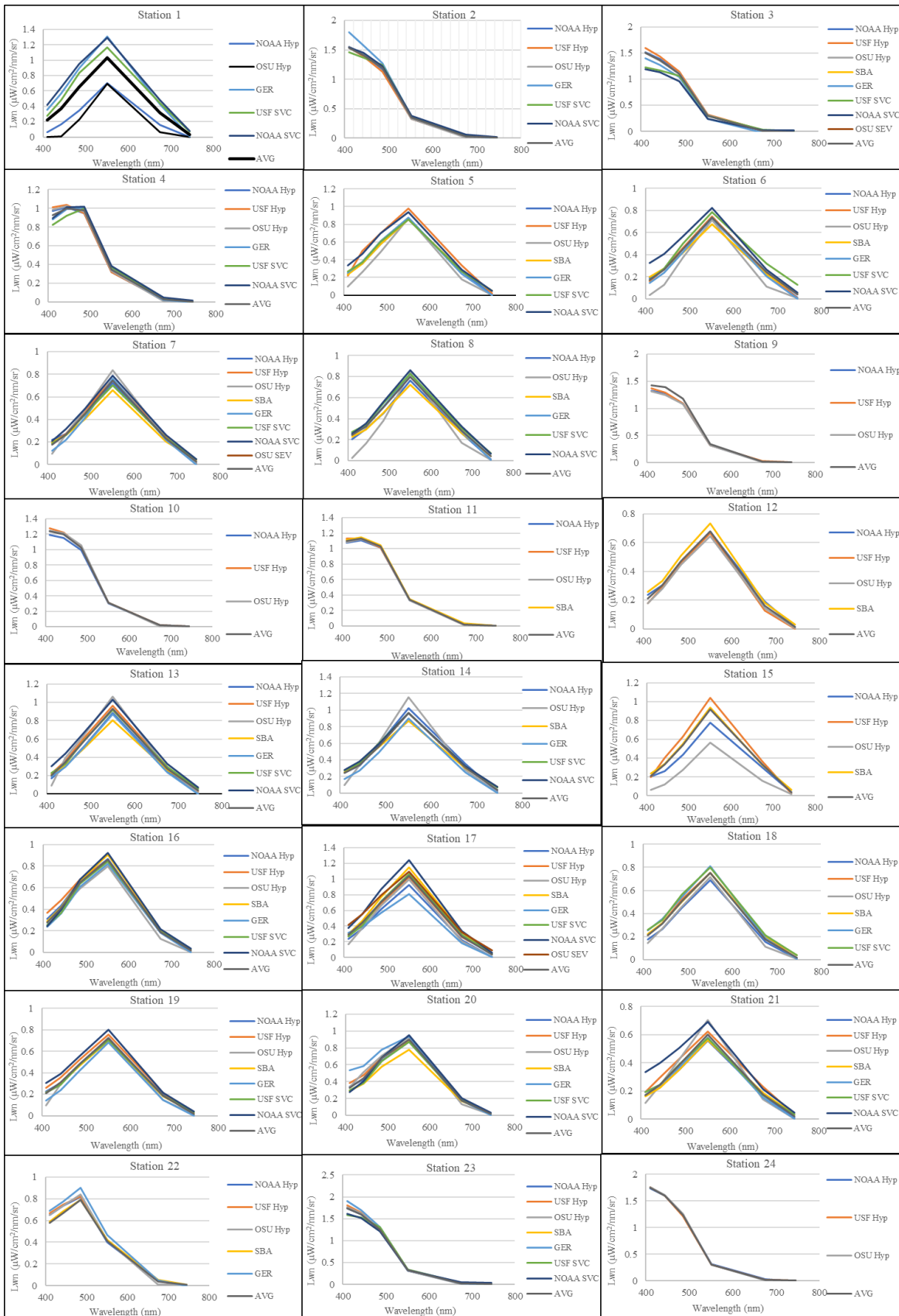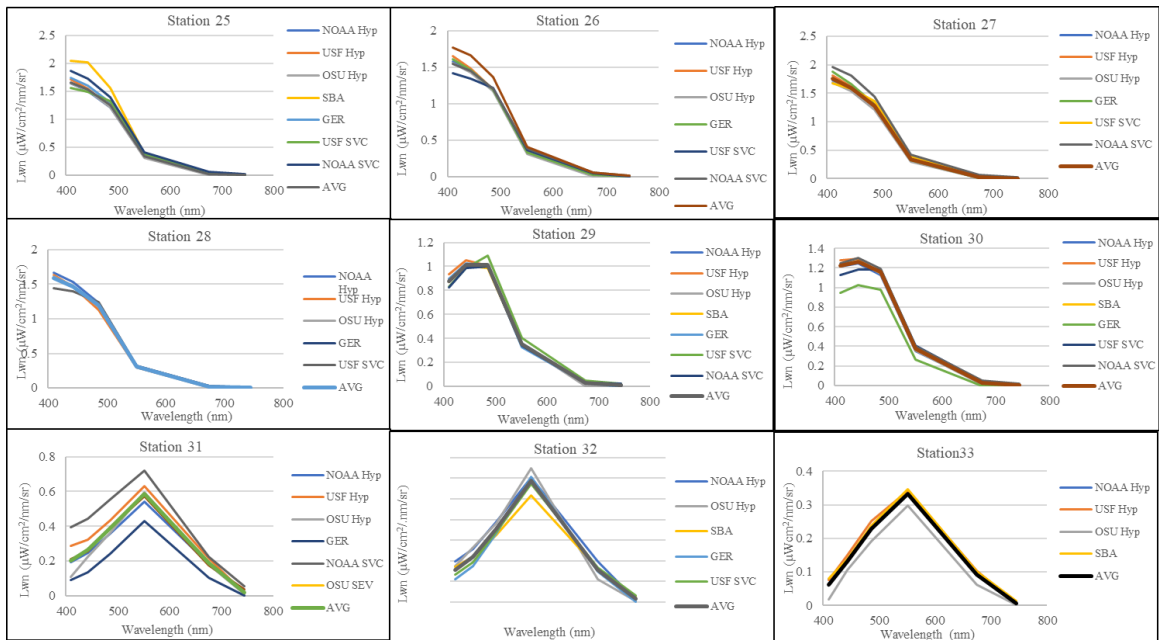
Figure 30. Example of the pre- and post-cruise calibration results for the NOAA/STAR L_u 206 radiance sensor (left) along with expected values for the lamp and (right) the percent difference between the expected lamp values and those measured by the radiometers.

To assess the performance of the VIIRS ocean color satellite sensors during this cruise, we compared the VIIRS SNPP and NOAA-20 $nL_w(\lambda)$ with in situ data for each station. VIIRS data were processed by the STAR ocean color science team using MSL12. The processing version for SNPP was NPPSCINIR_L2; SCI_OC04.0_v1.21, and the version for NOAA-20 was J01_SCINIR_L2; SCI_OC4.0_v1.21_v1.30. The method for determining valid satellite data to use for matchups with in situ data follows Wang et al. (2009b). Briefly, for each in situ observation, $nL_w(\lambda)$ satellite data from a 5×5 pixel box centered on the in situ sampling location are obtained. The average and σ of the $nL_w(\lambda)$ values of the 25 pixels in the box are calculated. Next, values with 1.5 or greater σ from the average are omitted. If the count of the remaining "good" values is greater than 50% of the original count (i.e., 13 or more out of 25), the average and σ are recalculated for the remaining "good" pixels. These results are then matched with the in situ observations. For the in situ measurements, up to 8 instruments were used to measure water-leaving radiances as described in Section 5. To remove outliers in the in situ data, the average and σ were calculated for all the instruments utilized at each station. Then, for each wavelength band, any data that were greater than one σ were removed, and then the final average and σ were calculated. Spectral results for each station for the two VIIRS sensors and the quality average representation of all the in situ are shown in Figure 31.

41
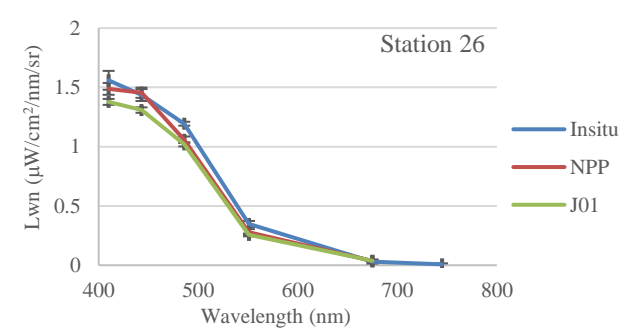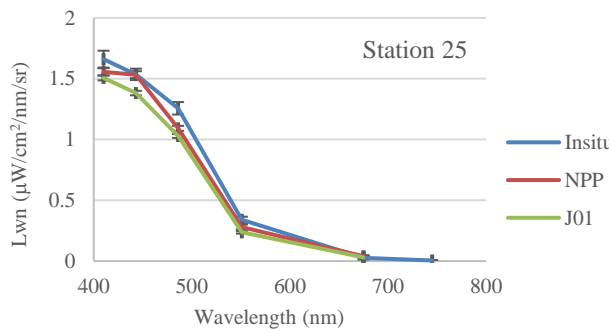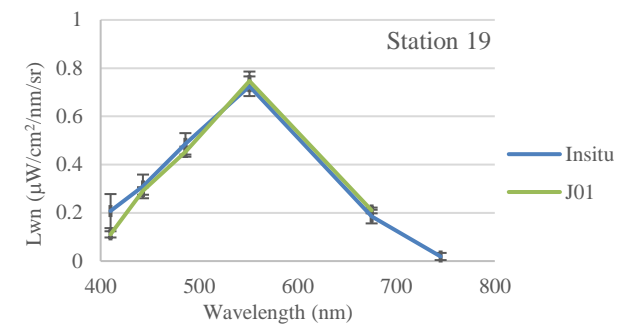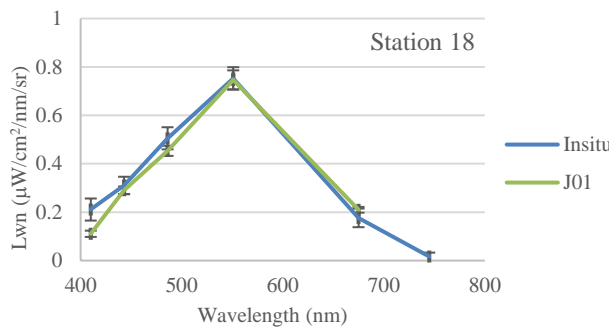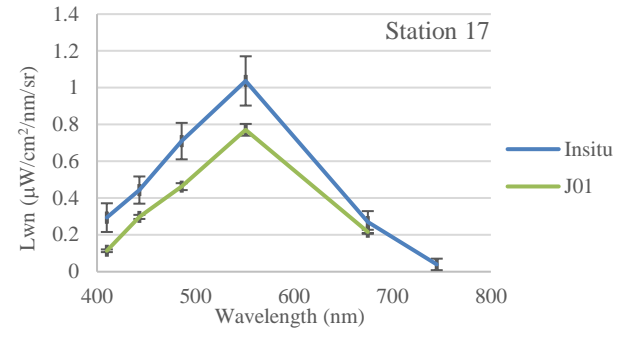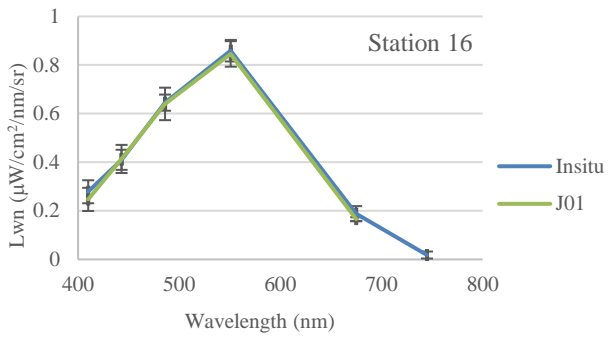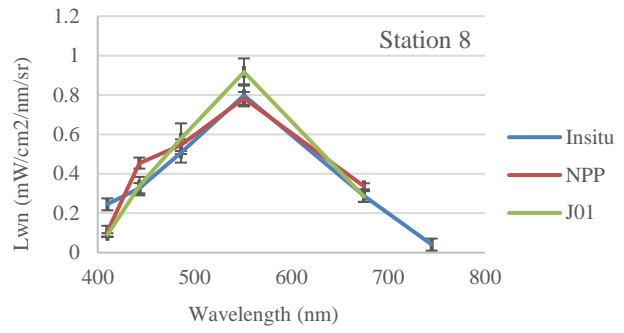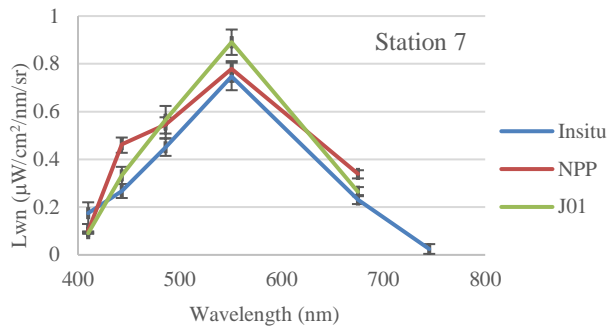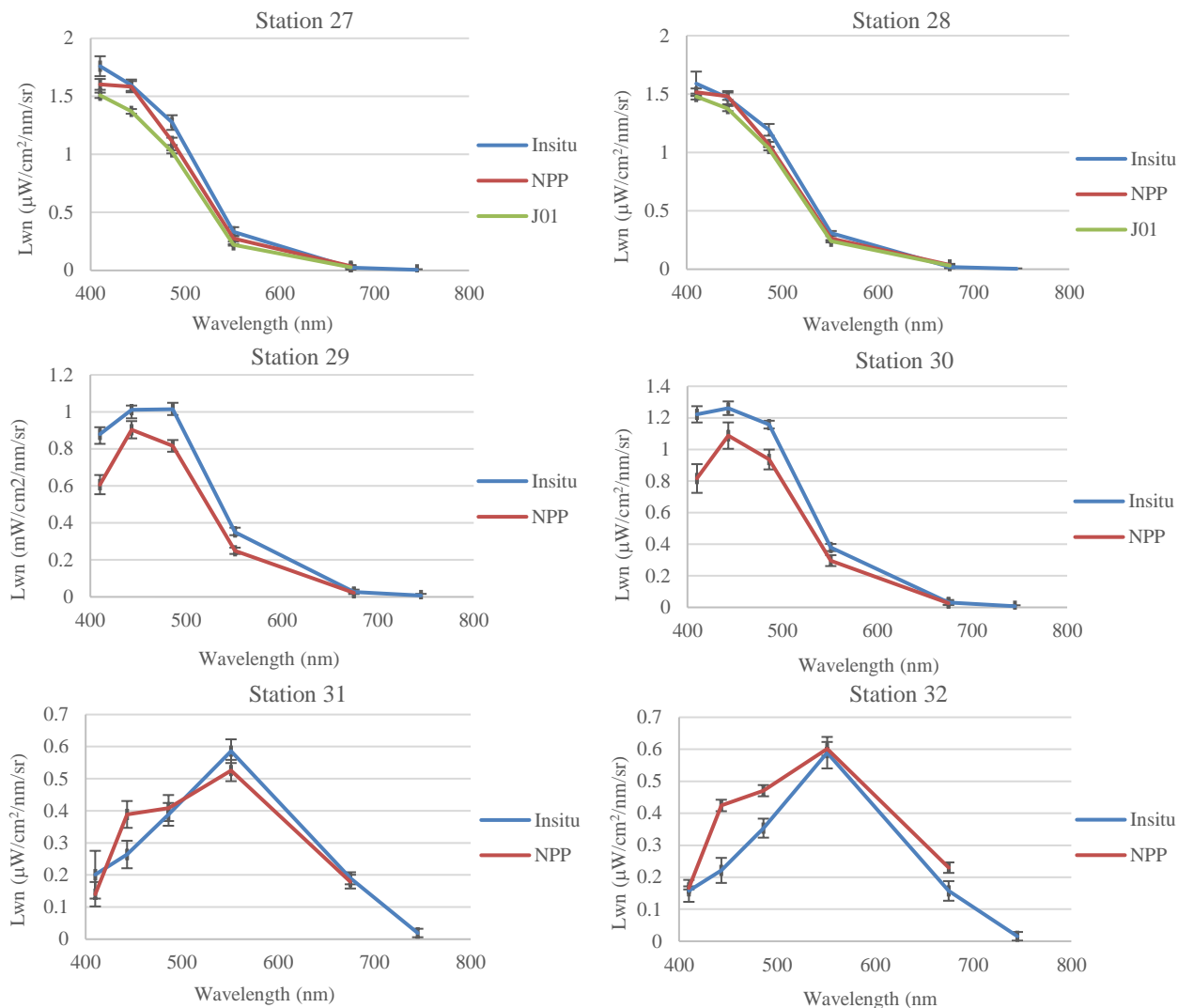
Figure 31. Preliminary MSL12 VIIRS 5 × 5 pixel average (SNPP, shown as NPP, in orange and NOAA-20, shown as J01, in green) versus the average for all in situ measurements (blue) at each station for stations where there were good matchups.

7. Conclusions

The 2021 ocean color Cal/Val cruise was carried out in a dynamic environment in the northern Gulf of Mexico. Over a ten-day period, the cruise generated high-quality measurements of radiometric quantities along with water inherent optical properties and biological and biogeochemical properties, allowing for constructing in situ and satellite matchups for the uncertainty assessment of the VIIRS products as well as the products from international sensors. These newly obtained data add to the existing in situ ocean color database, which can be used to cross-validate various in situ radiometry and water IOPs measurements. Furthermore, the cruise offers the opportunity to quantify the regional bio-optical complexity and develop regional bio-optical algorithms in the northern Gulf of Mexico. The in situ flow-through measurements, including the water IOPs and phytoplankton functional types, present further opportunities for satellite calibration and validation and studies of oceanic processes. In conclusion, this cruise was successful and reached the goals of the study. We look forward to a comprehensive analysis of the cruise data and sharing the data within the NOAA community and beyond.

References

Arnone, R., Fargion, G., Martinolich, P., Ladner, S., Lawson, A., Bowers, J., Ondrusek, M., Zibordi, G., Lee, Z., Trees, C., Davis, C., & Ahmed, S. (2012). Validation of the VIIRS ocean color. *Proc. SPIE, 8372*, https://doi.org/10.1117/12.922949

Arnone, R., Vandermeulen, R., Ladner, S., Bowers, J., Martinolich, P., Fargion, G., & Ondrusek, M. (2014). Sensitivity of calibration gains to ocean color processing in coastal and open waters using ensembles members for NPP-VIIRS. *Proc. SPIE, 9111*, https://doi.org/10.1117/12.2053409

Carder, K.L., & Steward, R.G. (1985). A remote-sensing reflectance model of a red tide dinoflagellate off West Florida. *Limnology and Oceanography, 30*, 286-298

Chekalyuk, A., & Hafez, M.A. (2008). Advanced laser fluorometry of natural aquatic environments. *Limnology and oceanography, methods, 6*, 591

Chekalyuk, A.M., Landry, M.R., Goericke, R., Taylor, A.G., & Hafez, M.A. (2012). Laser fluorescence analysis of phytoplankton across a frontal zone in the California Current ecosystem. *Journal of Plankton Research, 34*, 761-777, https://doi.org/10.1093/plankt/fbs034

Clark, D.K., Gordon, H.R., Voss, K.J., Ge, Y., Broenkow, W., & Trees, C. (1997). Validation of atmospheric correction over the oceans. *Journal of Geophysical Research-Atmospheres, 102*, 17209-17217, https://doi.org/10.1029/96jd03345

Cox, C., & Munk, W. (1954). Measurement of the roughness of the sea surface from photographs of the sun's glitter. *Journal of the Optical Society of America, 44*, 838-850

D'Sa, E.J., Miller, R.L., & McKee, B.A. (2007). Suspended particulate matter dynamics in coastal waters from ocean color: Applications to the Northern Gulf of Mexico. *Geophysical Research Letters, 34*, https://doi.org/10.1029/2007GL031192

Davis, C.O., Kavanaugh, M., Letelier, R., Bissett, W.P., & Kohler, D. (2007). Spatial and spectral resolution considerations for imaging coastal waters. *Proc. SPIE, 6680*, 66800P, 66801-66812.

EPA (1971). Methods for chemical analysis of water and wastes, EPA-NERL: 160.2. In: US Environmental Protection Agency.

Gege, P., & Grötsch, P. (2016). A spectral model for correcting sunglint and skyglint. In, *Ocean Optics XXIII* (pp. 1-10). Victoria, Kanada.

Gilerson, A., Carrizo, C., Malinowski, M., Groetsch, P., Foster, R., & Herrera Estrella, E. (2019). Multi- and hyperspectral polarimetric imaging of the ocean surface. *Proc. SPIE, 11150, Remote Sensing of the Ocean, Sea Ice, Coastal Waters, and Large Water Regions 2019, 1115007* (14 October 2019); https://doi.org/10.1117/12.2534055.

Goes, J.I., Gomes, H.d.R., Haugen, E.M., McKee, K.T., D'Sa, E.J., Chekalyuk, A.M., Stoecker, D.K., Stabeno, P.J., Saitoh, S.-I., & Sambrotto, R.N. (2014). Fluorescence, pigment and microscopic characterization of Bering Sea phytoplankton community structure and photosynthetic competency in the presence of a Cold Pool during summer. *Deep Sea Research Part II: Topical Studies in Oceanography, 109*, 84-99, https://doi.org/10.1016/j.dsr2.2013.12.004

Gorbunov, M.Y., & Falkowski, P.G. (2004). Fluorescence induction and relaxation (FIRe) technique and instrumentation for monitoring photosynthetic processes and primary production in aquatic

ecosystems. In, *Photosynthesis: Fundamental Aspects to Global Perspectives"-Proc. 13th International Congress of Photosynthesis, Montreal, Aug* (pp. 1029-1031)

Gordon, H.R., Clark, D.K., Mueller, J.L., & Hovis, W.A. (1980). Phytoplankton Pigments from the Nimbus-7 Coastal Zone Color Scanner: Comparisons with Surface Measurements. *Science, 210*, 63-66.

Groetsch, P.M.M., Foster, R., & Gilerson, A. (2020). Exploring the limits for sky and sun glint correction of hyperspectral above-surface reflectance observations. *Applied Optics, 59*, 2942-2954, https://doi.org/10.1364/AO.385853

Groetsch, P.M.M., Gege, P., Simis, S.G.H., Eleveld, M.A., & Peters, S.W.M. (2017). Validation of a spectral correction procedure for sun and sky reflections in above-water reflectance measurements. *Optics Express, 25*, A742-A761, https://doi.org/10.1364/OE.25.00A742

Holm-Hansen, O., & Riemann, B. (1978). Chlorophyll a determination: improvements in methodology. *Oikos, 30*, 438-447.

Hovis, W.A., Clark, D.K., Anderson, F., Austin, R.W., Wilson, W.H., Baker, E.T., Ball, D., Gordon, H.R., Mueller, J.L., El-Sayed, S.Z., Sturm, B., Wrigley, R.C., & Yentsch, C.S. (1980). Nimbus-7 Coastal Zone Color Scanner: System Description and Initial Imagery. *Science, 210*, 60-63.

Hunter, C. (2006). Particulate organic carbon, nitrogen and total suspended matter. Methodologies, protocols and analyses used in the development of ocean color product algorithms. In, *Technical Publication 06–1*: Moss Landing Marine Laboratories.

IOCCG (2010). Atmospheric correction for remotely-sensed ocean color products. In M. Wang (Ed.) (p. 78). Dartmouth, Nova Scotia, Canada: International Ocean Color Coordinating Group. https://doi.org/10.25607/OBP-101

Jenkins, C., Goes, J., McKee, K., Gomes, H.d.R., Arnone, R., Wang, M., Ondrusek, M., Nagamani, P., Preethi Latha, T., Rao, K., & Dadhwal, V. (2016). High-resolution shipboard measurements of phytoplankton: a way forward for enhancing the utility of satellite SST and chlorophyll for mapping microscale features and frontal zones in coastal waters. *Proc. SPIE* 9878, *Remote Sensing of the Oceans and Inland Waters: Techniques, Applications, and Challenges,* 98780U (May 7, 2016). http://dx.doi.org/10.1117/12.2225875

Jolliff, J.K., Jarosz, E., Ladner, S., Smith, T., Anderson, S., & Dykes, J. (2018a). The Optical Signature of a Bottom Boundary Layer Ventilation Event in the Northern Gulf of Mexico's Hypoxic Zone. *Geophysical Research Letters, 45*, 8390-8398, https://doi.org/10.1029/2018GL078228

Jolliff, J.K., Ladner, S., Lewis, D., Jarosz, E., Lawson, A., Smith, T., Penko, A., & McCarthy, S. (2018b). Hyperspectral determination of ocean color as an ocean monitoring tool: example applications in the Gulf of Mexico. *Proc. SPIE, 10631.*

Kishino, M., Takahashi, M., Okami, N., & Ichimura, S. (1985). Estimation of the spectral absorption coefficients of phytoplankton in the sea. *Bulletin of Marine Science, 37*, 634-642.

Lee, Z.P., Du, K., & Arnone, R. (2005). A model for the diffuse attenuation coefficient of downwelling irradiance. *Journal of Geophysical Research, 110*, https://doi.org/1029/2004JC002275

Lee, Z.P., Wei, J., Shang, Z., Garcia, R., Dierssen, H.M., Ishizaka, J., & Castagna, A. (2019). On-water radiometry measurements: skylight-blocked approach and data processing. In G. Zibordi, K.J. Voss, B.C. Johnson, & J.L. Mueller (Eds.), *Appendix to Protocols for Satellite Ocean Colour Data Validation: In Situ Optical Radiometry. IOCCG Ocean Optics and Biogeochemistry Protocols for Satellite Ocean Colour Sensor Validation, Volume 3.0* (p. 7). Dartmouth, NS, Canada: IOCCG

Mikelsons, K., & Wang, M. (2018). Interactive online maps make satellite ocean data accessible (https://www.star.nesdis.noaa.gov/socd/mecb/color/ocview/ocview.html). *Eos,* **99**, 01 May 2018, https://doi.org/10.1029/2018EO096563.

Mobley, C.D. (1999). Estimation of the remote-sensing reflectance from above-surface measurements. *Applied Optics, 38*, 7442-7455.

Mobley, C.D. (2015). Polarized reflectance and transmittance properties of windblown sea surfaces. *Applied Optics, 54*, 4828-4849, https://doi.org/10.1364/AO.54.004828

Moisan, T.A., Rufty, K.M., Moisan, J.R., & Linkswiler, M.A. (2017). Satellite observations of phytoplankton functional type spatial distributions, phenology, diversity, and ecotones. *Frontiers in Marine Science, 4*, https://doi.org/10.3389/fmars.2017.00189

Mueller, J., Fargion, G., & McClain, C.R. (2003a). Ocean optics protocols for satellite ocean color validation, Revision 4, Volume IV: Inherent optical properties: instruments, characterizations, field measurements and data analysis protocols. In (p. 76). Greenbelf, Maryland: National Aeronautical and Space Administration, Goddard Space Flight Space Center.

Mueller, J.L. (2000). SeaWiFS algorithm for the diffuse attenuation coefficient, K(490), using water-leaving radiances at 490 and 555 nm. In S.B. Hooker (Ed.), *SeaWiFS Postlaunch Calibration and Validation Analyses, Part 3* (pp. 24-27).

Mueller, J.L. (2003). In-water radiometric profile measurements and data analysis protocols. In J.L. Mueller, G.S. Fargion, & C.R. McClain (Eds.), *Ocean Optics Protocols for Satellite Ocean Color Sensor Validation, Revision 4* (p. 78). Greenbelt, Maryland: National Aeronautical and Space Administration, Goddard Space Flight Space Center.

Mueller, J.L., Davis, C., Arnone, R., Frouin, R., Carder, K.L., Lee, Z.P., Steward, R.G., Hooker, S., Mobley, C.D., & McLean, S. (2002). Above-water radiance and remote sensing reflectance measurement and analysis protocols. In J.L. Mueller, & G.S. Fargion (Eds.), *Ocean Optics Protocols for Satellite Ocean Color Sensor Validation, Revision 3, NASA/TM-2002-210004* (pp. 171-182).

Mueller, J.L., Davis, C.O., Arnone, R., Frouin, R., Carder, K., Lee, Z.P., Steward, R.G., Hooker, S.B., Mobley, C.D., & McLean, S. (2003b). Above-water radiance and remote sensing reflectance measurement and analysis protocols. In J.L. Mueller, G.S. Fargion, & C. McClain (Eds.), *Ocean Optics Protocols For Satellite Ocean Color Sensor Validation, Revison 4, Volume III: Radiometric Measurements and Data Analysis Protocols* (pp. 21 - 31). Greenbelt, Maryland: Goddard Space Flight Center, National Aeronautics and Space Administration.

Nalli, N. R., G. R. Foltz, J. Gero, L. Gibson, R. O. Knuteson, R. Lumpkin, P. J. Minnett, V. R. Morris, M. Ondrusek, R. C. Perez, M. Wang, and J. Wei (2022), "Chapter 11 – Ship-based cal/val campaigns," in book *Field Measurements for Passive Environmental Remote Sensing*, N. R. Nalli, (Ed.), p.195–217, ISBN: 978-0-12-823953-7, 436 pp., Elsevier. https://doi.org/10.1016/B978-0-12-823953-7.00008-3

O'Reilly, J.E., & Werdell, P.J. (2019). Chlorophyll algorithms for ocean color sensors - OC4, OC5 & OC6. *Remote Sensing of Environment, 229*, 32-47, https://doi.org/10.1016/j.rse.2019.04.021

Ondrusek, M., Lance, V.P., Wang, M., Arnone, R.A., Ladner, S., Goode, W., Vandermeulen, R., Freeman, S., Chaves, J.E., Mannino, A., Gilerson, A., Ahmed, S., Carrizo, C., El-Habashi, A., Foster, R., Ottaviani, M., Goes, J.I., Gomes, H.d.R., McKee, K., Hu, C., Kovach, C., English, D., Cannizzaro, J., Johnson, B.C., Lee, Z., Wei, J., Wang, Q., Lin, J., Tufillaro, N., Nahorniak, J., Davis, C.O., & Voss, K.J. (2015). Report for dedicated JPSS VIIRS Ocean Color Calibration/Validation Cruise. In V.P. Lance (Ed.), *NOAA technical report NESDIS 146* (p. 60). Washington, D.C.: NOAA National Environmental Satellite, Data, and Information Service. https://doi.org/10.7289/V52B8W0Z

Ondrusek, M., Lance, V.P., Wang, M., Arnone, R.A., Ladner, S., Goode, W., Vandermeulen, R., Freeman, S., Chaves, J.E., Mannino, A., Gilerson, A., Ahmed, S., Carrizo, C., El-Habashi, A., Foster, R., Ottaviani, M., Goes, J.I., Gomes, H.d.R., McKee, K., Hu, C., Kovach, C., English, D., Cannizzaro, J., Johnson, B.C., Lee, Z., Wei, J., Wang, Q., Lin, J., Tufillaro, N., Nahorniak, J., Davis, C.O., & Voss, K.J. (2016). Report for dedicated JPSS VIIRS Ocean Color December 2015 Calibration/Validation Cruise. In V.P. Lance (Ed.), *NOAA technical report NESDIS 148* (p. 66). Silver Spring, Maryland: United States, National Environmental Satellite, Data, and Information Service. https://doi.org/10.7289/V5/TR-NESDIS-148

Ondrusek, M., Lance, V.P., Wang, M., Stengel, E., Kovach, C., Arnone, R.A., Ladner, S., Goode, W., Gilerson, A., Ahmed, S.A., El-Habashi, A., Foster, R., Ottaviani, M., Goes, J.I., Gomes, H.d.R., McKee, K., Kang, J.W., Hu, C., Cannizzaro, J., Sun, S., English, D., Johnson, B.C., Lee, Z., Zoffoli, L., Lin, J., Tufillaro, N., Lalovic, I., Nahorniak, J., Davis, C.O., Twardowski, M., Stockley, N., & Voss, K.J. (2017). Report for dedicated JPSS VIIRS Ocean Color Calibration/Validation Cruise,

October 2016. In V.P. Lance (Ed.), *NOAA technical report NESDIS 151* (p. 65). Washington, D.C.: United States. National Environmental Satellite, Data, and Information Service. https://doi.org/10.7289/V5/TR-NESDIS-151

Ondrusek, M., Lance, V.P., Wang, M., Stengel, E., Kovach, C., Arnone, R.A., Ladner, S., Goode, W., Gilerson, A., El-Habashi, A., Carrizo, C., Herrera, E., Ahmed, S.A., Goes, J.I., Gomes, H.d.R., McKee, K., Hu, C., Cannizzaro, J., Zhang, Y., Huang, C.-W., English, D., Johnson, B.C., Lee, Z., Yu, X., Shang, Z., Tufillaro, N., Lalovic, I., & Voss, K.J. (2019). Report for Dedicated JPSS VIIRS Ocean Color Calibration/Validation Cruise May 2018. In V.P. Lance (Ed.), *NOAA technical report NESDIS 152* (p. 91). Washington, D.C.: United States. National Environmental Satellite, Data, and Information Service. https://doi.org/10.25923/scyb-qf42

Perez, R. C., G. R. Foltz, R. Lumpkin, J. Wei, K. J. Voss, M. Ondrusek, M. Wang, and M. Bourassa (2022), "Chapter 5 – Oceanographic buoys: Providing ocean data to assess the accuracy of variables derived from satellite measurements," in book *Field Measurements for Passive Environmental Remote Sensing*, N. R. Nalli, (Ed.), p.79–100, ISBN: 978-0-12-823953-7, 436 pp., Elsevier. https://doi.org/10.1016/B978-0-12-823953-7.00022-8

Pitarch, J., Talone, M., Zibordi, G., & Groetsch, P. (2020). Determination of the remote-sensing reflectance from above-water measurements with the "3C model": a further assessment. *Optics Express, 28*, 15885-15906.

Pope, R.M., & Fry, E.S. (1997). Absorption spectrum (380-700 nm) of pure water .2. Integrating cavity measurements. *Applied Optics, 36*, 8710-8723.

Rabalais, N.N., Turner, R.E., & Wiseman, W.J. (2002). Gulf of Mexico Hypoxia, a.k.a. "The Dead Zone". *Annual Review of Ecology and Systematics, 33*, 235-263.

Röttgers, R., McKee, D., & Woźniak, S.B. (2013). Evaluation of scatter corrections for ac-9 absorption measurements in coastal waters. *Methods in Oceanography, 7*, 21-39.

Ruddick, K.G., Voss, K., Boss, E., Castagna, A., Frouin, R., Gilerson, A., Hieronymi, M., Johnson, B.C., Kuusk, J., Lee, Z., Ondrusek, M., Vabson, V., & Vendt, R. (2019). A review of protocols for fiducial reference measurements of water-leaving radiance for validation of satellite remote-sensing data over water. *Remote Sensing, 11*, 2198, https://doi.org/10.3390/rs11192198.

Satlantic (2003). Operation Manual for Profiler II. In. Halifax, Nova Scotia: Satlantic Incorporated.

Satlantic (2004). SatView Data Logging / Display Program Users Guide; Version 2.8. In. Halifax, Nova Scotia: Satlantic Incorporated.

Tufillaro, N. (2022). Correlation of remote sensing water quality maps with an in situ sensor network, DOE report on grant DE-SC0020843.

Van Heukelem, L., & Thomas, C.S. (2001). Computer-assisted high-performance liquid chromatography method development with applications to the isolation and analysis of phytoplankton pigments. *Journal of Chromatography A, 910*, 31-49, https://doi.org/10.1016/s0378-4347(00)00603-4

Vandermeulen, R.A., Mannino, A., Craig, S.E., & Werdell, P.J. (2020). 150 shades of green: Using the full spectrum of remote sensing reflectance to elucidate color shifts in the ocean. *Remote Sensing of Environment, 247*, 111900, https://doi.org/10.1016/j.rse.2020.111900

Vanhellemont, Q. (2019). Adaptation of the dark spectrum fitting atmospheric correction for aquatic applications of the Landsat and Sentinel-2 archives. *Remote Sensing of Environment, 225*, 175-192, https://doi.org/10.1016/j.rse.2019.03.010

Walsh, J.J., Jolliff, J.K., Darrow, B.P., Lenes, J.M., Milroy, S.P., Remsen, A., Dieterle, D.A., Carder, K.L., Chen, F.R., Vargo, G.A., Weisberg, R.H., Fanning, K.A., Muller-Karger, F.E., Shinn, E., Steidinger, K.A., Heil, C.A., Tomas, C.R., Prospero, J.S., Lee, T.N., Kirkpatrick, G.J., Whitledge, T.E., Stockwell, D.A., Villareal, T.A., Jochens, A.E., & Bontempi, P.S. (2006). Red tides in the Gulf of Mexico: Where, when, and why? *Journal of Geophysical Research, 111*, https://doi.org/10.1029/2004JC002813

Wang, M., & Jiang, L. (2018). Atmospheric correction using the information from the short blue band. *IEEE Transactions on Geoscience and Remote Sensing, 56*, 6224-6237.

Wang, M., Liu, X., Jiang, L., Son, S., Sun, J., Shi, W., Tan, L., Naik, P., Mikelsons, K., Wang, X., & Lance, V. (2014). Evaluation of VIIRS Ocean Color Products. *Proc. SPIE 9261, 92610E*, http://dx.doi.org/10.1117/12.2069251

Wang, M., Liu, X., Tan, L., Jiang, L., Son, S., Shi, W., Rausch, K., & Voss, K. (2013). Impact of VIIRS SDR performance on ocean color products. *J. Geophys. Res. Atmos., 118*, 10347–10360, https://doi.org/10.1002/jgrd.50793

Wang, M., & Son, S. (2016). VIIRS-derived chlorophyll-a using the ocean color index method. *Remote Sensing of Environment, 182*, 141-149, https://doi.org/10.1016/j.rse.2016.05.001

Wang, M., Son, S., & Harding, L.W. (2009a). Retrieval of diffuse attenuation coefficient in the Chesapeake Bay and turbid ocean regions for satellite ocean color applications. *Journal of Geophysical Research, 114*, https://doi.org/10.1029/2009JC005286

Wang, M., Son, S., & Shi, W. (2009b). Evaluation of MODIS SWIR and NIR-SWIR atmospheric correction algorithm using SeaBASS data. *Remote Sensing of Environment, 113*, 635-644.

Wei, J., Wang, M., Jiang, L., Yu, X., Mikelsons, K., & Shen, F. (2021a). Global estimation of suspended particulate matter from satellite ocean color imagery. *Journal of Geophysical Research, 126*, e2021JC017303, https://doi.org/10.1029/2021JC017303

Wei, J., Wang, M., Lee, Z.P., Ondrusek, M., Zhang, S., & Ladner, S. (2021b). Experimental analysis of the measurement precision in spectral water-leaving radiance in different water types. *Optics Express, 29*, 2780-2797, https://doi.org/10.1364/OE.413784

Wei, J., Wang, M., Mikelsons, K., Jiang, L., Kratzer, S., Lee, Z.P., Moore, T., Sosik, H.M., & Van der Zande, D. (2022a). Global satellite water classification data products over oceanic, coastal, and inland waters. *Remote Sensing of Environment, 282*, 113233, https://doi.org/10.1016/j.rse.2022.113233

Wei, J., M. Wang, M. Ondrusek, A. Gilerson, J. Goes, C. Hu, Z. Lee, K. J. Voss, S. Ladner, V. P. Lance, and N. Tufillaro (2022b), "Chapter 20 – Satellite ocean color validation," in book *Field Measurements for Passive Environmental Remote Sensing*, N. R. Nalli, (Ed.), p.351–374, ISBN: 978-0-12-823953-7, 436 pp., Elsevier. https://doi.org/10.1016/B978-0-12-823953-7.00006-X

Wei, J., Yu, X., Lee, Z.P., Wang, M., & Jiang, L. (2020). Improving low-quality satellite remote sensing reflectance at blue bands over coastal and inland waters. *Remote Sensing of Environment, 250*, 112029, https://doi.org/10.1016/j.rse.2020.112029

Welschmeyer, N.A. (1994). Fluorometric analysis of chlorophyll-*a* in the presence of chlorophyll-*b* and pheopigments. *Limnology and Oceanography, 39*, 1985-1992.

WETLabs (2011). ac meter protocol document. In, *ac meter protocol (acprot); Revision Q 20 April 2011*

Zaneveld, J.R.V., Kitchen, J.C., & Moore, C.C. (1994). Scattering error correction of reflecting-tube absorption meters. Proc. SPIE 2258, Ocean Optics XII, (26 October 1994); doi:10.1117/12.190095.

Zappa, C.J., Banner, M.L., Schultz, H., Corrada-Emmanuel, A., Wolff, L.B., & Yalcin, J. (2008). Retrieval of short ocean wave slope using polarimetric imaging. *Measurement Science and Technology, 19*, 055503, doi:10.1088/0957-0233/19/5/055503.

Zibordi, G., Mélin, F., Berthon, J.-F., Holben, B., Slutsker, I., Giles, D., D'Alimonte, D., Vandemark, D., Feng, H., Schuster, G., Fabbri, B.E., Kaitala, S., & Seppälä, J. (2009). AERONET-OC: A network for the validation of ocean color primary products. *Journal of Atmospheric and Oceanic Technology, 26*, 1634-1651. https://doi.org/10.1175/2009JTECHO654.1

Appendix – Abbreviations, Units and Acronyms

Table A1. Notations and descriptions used in this report.

Abbreviation	Description	Typical Units (if applicable)
a_d	Absorption coefficient of detrital matter	m^{-1}
AERONET-OC	Aerosol Robotic Network-Ocean Color	
a_g	Absorption coefficient due to gelbstoff (CDOM)	m^{-1}
AOPs	Apparent optical properties	
AOT	Aerosol optical thickness	
a_p	Absorption due to particles	m^{-1}
a_{pg}	Absorption due to particles plus gelbstoff (detrital matter)	m^{-1}
a_{ph}	Phytoplankton pigment absorption coefficient	m^{-1}
a^*_{ph}	Chlorophyll-specific phytoplankton absorption coefficient	$m^2\ mg^{-1}$
b_b	Backscattering (scattering in the backwards direction)	m^{-1}
β	Volume scattering function	
β_p	Volume scattering function of particles	
b_p	Scattering coefficient of particles	
Cal/Val	Calibration and Validation	
CCNY	City College of New York	
CDOM	Chromophoric dissolved organic material	ppb
Chl-a	Chlorophyll a concentration	$mg\ m^{-3}$
c_{pg}	Total (nonwater) attenuation coefficient	m^{-1}
CZCS	Coastal Zone Color Scanner instrument aboard the NIMBUS-7 satellite	
E_d	Downwelling irradiance	$mW\ cm^{-2}\ \mu m^{-1}$
EDR	Environmental Data Record	
E_s	Downwelling irradiance just above water surface	
FOV	Field of view	
GCOM-C	Global Climate Observation Mission-Climate	
GOM	Gulf of Mexico	
GPS	Global Positioning System	
HPLC	High Pressure Liquid Chromatography	
IOPs	Inherent optical properties	
JPSS	Joint Polar Satellite System (program)	
K_d	Downwelling diffuse attenuation coefficient	m^{-1}
LDEO	Lamont-Doherty Earth Observatory at Columbia University	
L_{surf}	Total radiance from water surface	$mW\ cm^{-2}\ \mu m^{-1}\ sr^{-1}$
L_{sky}	Radiance of sky	$mW\ cm^{-2}\ \mu m^{-1}\ sr^{-1}$
L_u	Upwelling radiance	$mW\ cm^{-2}\ \mu m^{-1}\ sr^{-1}$
$L_u(0^-, \lambda)$	Spectral upwelling radiance just below water surface	$mW\ cm^{-2}\ \mu m^{-1}\ sr^{-1}$
L_w	Water-leaving radiance	$mW\ cm^{-2}\ \mu m^{-1}\ sr^{-1}$
MOBY	Marine Optical BuoY	

MSL12	Multi-Sensor Level-1 to Level-2	
NASA	National Aeronautics and Space Agency	
NCEI	National Centers for Environmental Information	
NESDIS	National Environmental Satellite, Data, and Information Service	
NIR	Near infrared	
NIST	National Institute of Standards and Technology	
nL_w	Normalized water-leaving radiance	$mW\ cm^{-2}\ \mu m^{-1}\ sr^{-1}$
NRL	Naval Research Laboratory	
NOAA	National Oceanic and Atmospheric Administration	
OC	Ocean Color	
OCI	Ocean Color Irradiance	
OCR	Ocean Colour Radiance	
OCST	Ocean Color Science Team	
OLCI	Ocean and Land Colour Instrument	
OMAO	Office of Marine and Air Operations	
OSU	Oregon State University	
PFT	Phytoplankton Functional Type	
R_{rs}	Remote sensing reflectance	sr^{-1}
SBA	Skylight-blocking apparatus	
SGLI	Second Generation Global Imager	
SNPP	Suomi National Polar-orbiting Partnership	
STAR	Center for Satellite Applications and Research	
SPM	Suspended Particulate Matter	$mg\ L^{-1}$
UMB	University of Massachusetts – Boston	
USF	University of South Florida	
VIIRS	Visible Infrared Imaging Radiometer Suite	
w	Wind speed	m/s
λ	Wavelength	nm
φ	Relative azimuth of the sensor to the sun	°
ρ	Fresnel reflectance factor of seawater	
θ	Zenith Angle	°

Table A2. Instrument shorthand, description and manufacturer with modifications when applicable.

Instrument Shorthand	Full Identification/Purpose	Manufacturer or Citation
ac-9	In situ spectrophotometer - 9 channel resolution	WET Labs
ac-s	In situ spectrophotometer – high spectral resolution	WET Labs
ASD	Analytical Spectral Device; HandHeld2-Pro visible and near infrared spectrophotometer	PANalytical
BB-3	Backscatter – 3 channels	WET Labs
CTD	Conductivity, Temperature, Depth	Generic, various manufacturers
ECO BB9	Backscatter – 9 channels	WET Labs
FIRe	Variable fluorescence	Satlantic
FlowCam	Dynamic imaging particle analysis for species composition and size measurements	Fluid Imaging Technologies, Inc.
GER	Field portable spectroradiometer	Spectra Vista Corporation
HyperOCI	Hyperspectral irradiance sensor	Satlantic LP
HyperOCR	Hyperspectral radiance sensor	Satlantic LP
HyperPro, HyperPro-II	Free-falling hyperspectral optical profiler	Satlantic LP
Microtops	Handheld sun photometer (atmospheric aerosols and optical depth)	Solar Light Company
NuRads	Upwelling Radiance Distribution Camera System	Voss and Chapin, 2005